THE GEOLOGICAL SOCIETY OF AMERICA®

Influence of flow discharge and minibasin shape on the flow behavior and depositional mechanics of ponded turbidity currents

J. Kevin Reece[1,†], Robert M. Dorrell[2], and Kyle M. Straub[1]
[1]*Department of Earth and Environmental Sciences, Tulane University, New Orleans, Louisiana 70118, USA*
[2]*Energy and Environment Institute, University of Hull, Hull, HU6 7RX, UK*

ABSTRACT

The interplay between seafloor sediment-laden density-driven flows, turbidity currents, and topography helps to shape continental margins. However, these interactions are poorly understood, especially those within enclosed depressions termed minibasins. In this study, novel experiments quantify the three-dimensional (3-D) dynamics of turbidity currents interacting with a range of minibasin geometries that, for the first time, scale within the parameter space of natural systems. Controls on flow dynamics are quantified by measuring the evolving velocity and sediment transport fields, in addition to maps of bathymetry. This study focuses on three aspects of turbidity current interactions with minibasins. First, the results suggest that sediment transport and deposition in minibasins is likely dominated by evolving flow conditions. Contrary to earlier studies in two-dimensional (2-D) flumes, this study supports a time-to-flow equilibrium in minibasins that scales with the time to replace ambient fluid with turbid influx, and this replacement time likely takes days to achieve in many field-scale minibasins. Second, in all experiments, horizontal flow circulation is observed, which is critical for distributing sediment throughout minibasins. However, the strength of the horizontal circulation reduces as the ratio of minibasin length to width increases, which leads to stagnant or even upstream-directed flow near the bed, elevated height of the velocity maximum in flows, the lowering of near-bed shear stresses, and more homogeneous deposits through a reduction in bed reworking. Finally, the results indicate that fluid detrainment from minibasins significantly reduces sediment fall velocities, severely lowering the sediment-trapping efficiency for small or light particles. This reduction in effective fall velocities of sediments suggests a mechanism that fractionates fine particulates (e.g., clays), nutrients (e.g., organic carbon), and pollutants (e.g., microplastics) along transport paths down topographically complex margins.

INTRODUCTION

The structure of many continental margins reflects a competition between the dynamics of mobile substrates (Hudec and Jackson, 2007; Soto et al., 2021) and the processes that control sediment transport and deposition (Pirmez et al., 2000; Prather, 2003; Straub and Mohrig, 2009; Mitchell et al., 2021; Privat et al., 2024). Here, mobile substrates include uncompacted shales (van Rensbergen et al., 1999; Dinc et al., 2023) and salt (Hudec and Jackson, 2007) that can undergo ductile deformation if an overburden exceeds a critical mass for geological time scales. Some of these depressions are large enough to significantly influence the depositional mechanics of turbidity currents (Winker, 1996; Pirmez et al., 2012; Ge et al., 2020), which are the primary mechanism for transporting sediment into the deep sea (Talling et al., 2015, 2022). For example, movement of the mobile Louann salt along the northern continental margin of the Gulf of Mexico of southeastern North America has produced depressions called minibasins that have horizontal scales of up to tens of kilometers and relief of up to hundreds of meters (Hudec et al., 2013; Fig. 1). Minibasins can also be found offshore Brazil (Mohriak et al., 2012) and West Africa (Ge et al., 2020), as well as in the eastern Mediterranean (Zucker et al., 2020; Mousouliotis et al., 2021) and North Sea (Stricker et al., 2018). Flat minibasin floors and adverse slopes on distal walls that can exceed 10% reduce the driving gravitational force on flows, which reduces their sediment transport capacity and promotes deposition and the filling of minibasins (Beaubouef and Abreu, 2006; Prather et al., 2012). We note that along some margins, mobile substrates produce adverse slopes, but not depressions enclosed in three dimensions (3-D)—for example, shale ridges resulting from diapirism (Prather, 2003; Straub and Mohrig, 2009; Soto et al., 2021). Enhanced clastic deposition caused by these obstacles results in economically important geofluid reservoirs (e.g., hydrocarbons in their gas and liquid forms, as well as CO_2 and water; see Mohriak et al., 2012, and Stricker et al., 2018). Furthermore, such obstacles likely impact the transport, deposition, and preservation of particulate organic carbon (Talling et al., 2024) and other nutrients and pollutants impacting marine life (Kane et al., 2020).

In recent years, observations of turbidity currents at the field scale have increased due to technological advances (Xu et al., 2004; Vendettuoli et al., 2019; Simmons et al., 2020; Pope et al., 2022a; Talling et al., 2022). These observations are revolutionizing our understanding of the fluid and sediment transport mechanics of turbidity currents, and provide us with the ability to test theory developed largely from laboratory-scale observations. However, there are currently no field-scale flow measurements from settings with adverse topographic slopes caused by mobile substrates.

Given the relative lack of active flow measurements in minibasins and upstream of features such as shale ridges, knowledge of turbidity current interactions with topographic obstacles leverages stratigraphic observations from cores (Pirmez et al., 2012), well-logs (Alexander and Flemings, 1995), outcrops (Smith, 2004; Marini et al., 2016), and seismic data (Winker, 1996; Andresen et al., 2011; Prather et al., 2012). For example, the Brazos-Trinity system of linked minibasins offshore Texas, USA (Fig. 1), is one of the most studied minibasin systems, with observations leading to several competing models for the progressive filling of minibasins (Winker and Booth, 2000; Beaubouef, 2004; Beaubouef and Abreu, 2006; Pirmez et al., 2012; Prather et al., 2012). Suggested process-based models include (1) the fill-and-spill (Winker,

J. Kevin Reece https://orcid.org/0009-0009-3273-6016
[†]jreece@tulane.edu

GSA Bulletin; March/April 2025; v. 137; no. 3/4; p. 1797–1814; https://doi.org/10.1130/B37517.1.
Published online 13 November 2024

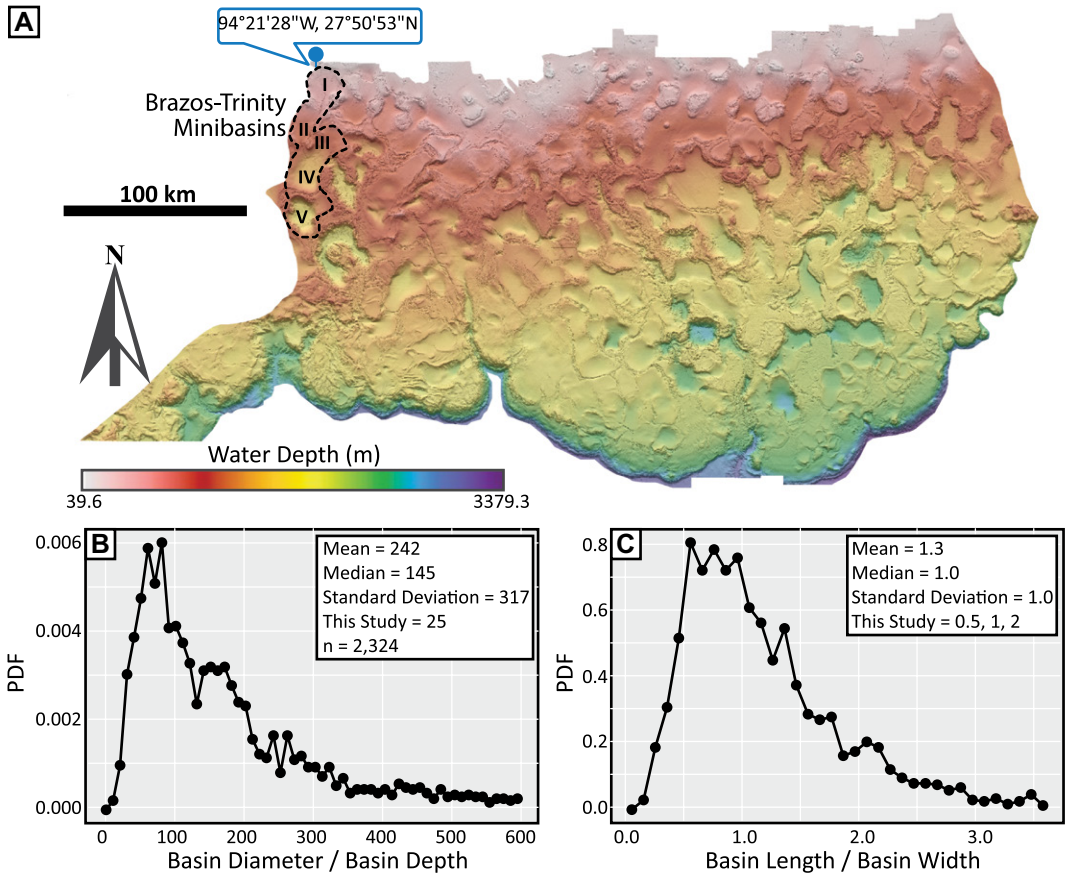

Figure 1. Map of the fill-and-spill region (Steffens et al., 2003) of the northern Gulf of Mexico and distributions that define geometries of enclosed minibasins. (A) Modified version of the high-resolution Gulf of Mexico Bureau of Ocean Energy Management bathymetric dataset (Kramer and Shedd, 2017) trimmed to the fill-and-spill region; a dashed line indicates the margin of the Brazos-Trinity minibasin system. (B) Distribution of minibasin diameter to depth, where minibasins are defined as local seafloor depressions with a surface area of >1 km². (C) Distribution of minibasin length to width, where length is measured from north to south (regional primary flow direction) and width is measured from east to west.

1996) model, where upstream minibasins capture 100% of flow until reaching a spill point and then sending all flow to downstream basins; and (2) the flow-stripping (Badalini et al., 2000) model, where upper portions of ponded flows in proximal basins can be stripped over confining sills and leak to downslope minibasins.

Models for the filling of depressions by turbidity currents and the flow behavior of ponded turbidity currents have been tested with physical experiments performed at reduced scale and numerical models. We highlight a set of experiments performed in narrow flumes meant to suppress 3-D flow dynamics (Lamb et al., 2004, 2006; Toniolo et al., 2006b; Patacci et al., 2015) or that utilized 2-D numerical solvers for down-system and vertical flow structure (Bastianon et al., 2021). As minibasins are inherently 3-D, hydrodynamics and thus depositional features must depend on all three components of flow. Therefore, the aim of this work is to study turbidity current flows and deposits in a 3-D physical experimental setup by testing predictions and observations emanating from prior 2-D studies.

The first theoretical prediction centers on the time necessary for sustained flows entering minibasins to achieve equilibrium conditions in minibasins. Observations from 2-D experiments supported a theory that predicts an equilibrium time based on the length of minibasins and the speed of an upstream-migrating bore that results from flow interaction with a distal minibasin wall (Lamb et al., 2004). Application of this theory to field-scale minibasins suggested that flows entering minibasins could reach equilibrium in approximately one hour. Thus, the deposits of flows with sustained conditions for days, as has been argued along some margins (Imran et al., 1999; Pirmez and Imran, 2003), would be dominated by the equilibrium flow field. If this is the case, the inversion of deposit structure for environmental parameters encoded in flow forcing conditions may be straightforward.

Second, flume experiments identified the development of flow circulation in minibasins, with upstream-directed flow riding above a lower layer directed down system (Patacci et al., 2015). The structure and direction of this circulation influences the fluid stress on the sediment bed and thus the sediment transport capacity of turbidity currents within minibasins. However, Bastianon et al. (2021), who performed a 2-D numerical study of turbidity currents in minibasins, noted the likely importance of lateral flow expansion in the third dimension to the style and magnitude of fluid circulation in minibasins. Lateral circulation was recently documented by Reece et al. (2024), who highlighted its importance for distributing sediment throughout circular minibasins and identified upwelling in the center of the cells, with implications for the sediment-trapping potential of minibasins. This suggests that the planform shape of minibasins should influence the partitioning of circulation along vertical-versus-horizontal planes. However, the influence of minibasin length to width on this partitioning remains unexplored, and it can vary substantially across salt provinces.

Third, observations from quasi 2-D experiments supported a theory for prediction of the sediment-trapping potential of minibasins. Trapping potential was theorized to equate to the product of the still-fluid settling velocity of sediment in transport and the surface area of a minibasin (Lamb et al., 2006; Toniolo et al., 2006a). This theory, based on analogy to a decanting process, has implications for our ability to predict the mass transport down-complex margins and the progressive fractionation of mass based on grain size in sequences of linked minibasins. For example, a core through the Basin IV Quaternary fan of the Brazos-Trinity minibasin system has a total organic carbon (TOC) content of 0.53 wt% (Flemings et al., 2006), a value

greater than has been measured in some modern Gulf of Mexico deltas (Shields et al., 2017). This highlights the importance of submarine fans to the global carbon cycle (Talling et al., 2024). It is unclear, though, if this value is characteristic of all deposits in the Brazos-Trinity system, or if there is a systematic trend in organic content from proximal to distal minibasins set by the size and settling velocity of particulate organic carbon relative to the clastic fill.

To examine these three questions, the flow behavior within experimental 3-D minibasins was monitored to understand its impact on depositional mechanics. This study reports results from two sets of physical experiments. The first set (discharge series) focused on variations in the volumetric discharge delivered to minibasins, with conditions ranging from near complete flow containment to those that produced significant flow stripping and only partial containment. The second set of experiments explored how the ratio of minibasin length to width influences the circulation of fluid in minibasins, with implications for sediment transport.

METHODS

Experimental Design

The experimental design was motivated by the bathymetry of the northern Gulf of Mexico and scales of depressions extracted from the Bureau of Ocean Energy Management's northern Gulf of Mexico bathymetric grid generated from 3-D seismic surveys (Kramer and Shedd, 2017) within lab-scale feasibility. Isolating an analysis to the fill-and-spill region defined in Steffens et al. (2003; Fig. 1) and using standard ArcGIS hydrological toolsets (Planchon and Darboux, 2002; Wang and Liu, 2006), all local depressions with planform areas >1 km^2 were identified. The depressions (n = 2324) have scales set by enclosed topography below the elevation of rims (i.e., spill points). Distributions were generated for the diameter to depth and length to width of depressions, where depression length was aligned with the regional down-dip flow direction (north-to-south), and width was measured perpendicular to this (Figs. 1B and 1C). Median depression diameter to depth is 145 and ranges from 14 to 3400, with a mode of 90. These widths and depths suggest depression sidewall slopes of between 0.1% and 14% (median = 1.4%, mode = 2.2%). The median depression length to width is 1.0 and ranges between 0.1 and 11.8, with a mode of 0.75.

Prior 3-D experiments have explored turbidity current–minibasin interactions. These include experiments focused on the architecture of turbidites deposited with ongoing subsidence (but essentially no data to define flow parameters; Violet et al., 2005) and a set of unpublished studies performed in minibasins of relatively small scale (minibasin width ≤1 m; Maharaj, 2012; Bastianon, 2018). The small minibasin widths made it difficult to capture the 3-D flow field given the measurement footprint of typical velocity profilers. Furthermore, minibasin sidewall slopes in these experiments (between 27% and 70%) were significantly greater than those observed in the field (generally <10%). Matching field-scale sidewall slopes at experimental scale is important as shallower sidewall slopes decrease both the thickness of deposits and the capability to pond and inflate flows, due to detrainment scaling with the ponded area (Dorrell et al., 2018). Recent work also suggests that adverse slopes >17% cause reflection of density underflows in the opposite direction, as the slope acts as an obstacle to the current. In contrast, underflows interacting with lower slopes can convert their kinetic energy into potential energy, as they run up the adverse slope until they stall and establish an upstream-migrating bore (De Falco et al., 2020).

Minibasins were constructed within the Tulane University Deepwater Basin (Fig. 2), with dimensions that compare more favorably to field-scale systems than those of previous work. This basin is 6 m long, 4 m wide, and 2.2 m deep. Minibasins were carved into a deposit of sand with a grain size of 300 μm residing on a false floor surrounded on the lateral and distal

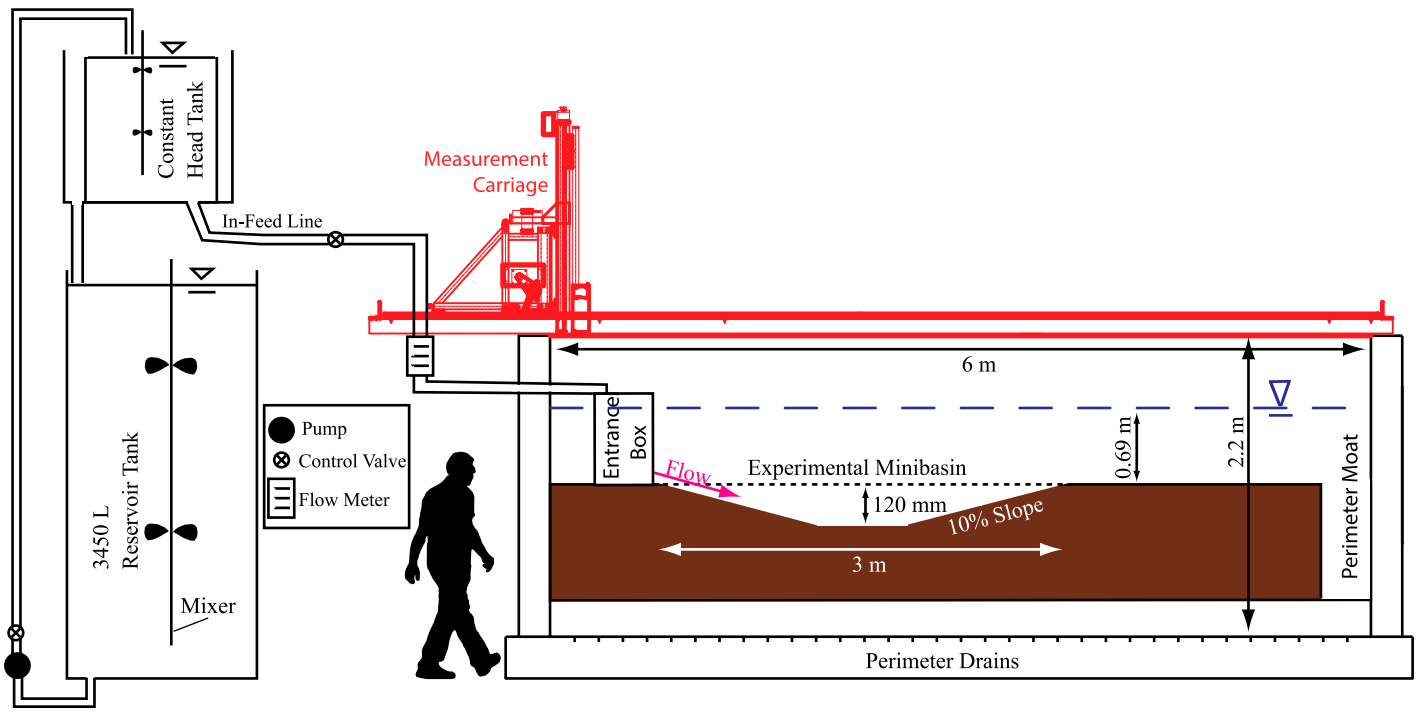

Figure 2. Schematic of experimental setup. Flux rate of slurry release to basin was controlled with a series of valves and monitored by a flow meter. False floor in basin with minibasin carved into 300 mm of sand is shown in brown, which is surrounded by a drainage moat. Dashed blue line shows elevation of water surface above bed. Schematic is not to scale.

sides by a 0.3-m-wide moat with a drainage system to prevent current reflections off deepwater basin walls. No evidence was found of reworking of the antecedent surface upon sectioning of the deposit, which suggests it was too coarse to be reworked by the experimental turbidity currents. Given the size constraints of the experimental basin, minibasins were designed with an average basin rim diameter of 3 m. Minibasins were either circular in planform (discharge series) or elliptical (aspect ratio series), with all minibasins having a planform area of 7.06 m^2. The depth of all minibasins was set to 0.12 m, resulting in a ratio of mean diameter to depth of 25. While on the low end of values observed in the Gulf of Mexico (Fig. 1B), the ratio of mean diameter to depth is within the natural spectrum and yields minibasin depths great enough to contain turbidity currents with thicknesses that allow flow properties to be measured. Thus, minibasins had a flat center, with an average diameter of 0.61 m. Crucially, the average ratio of the rim-to-rim basin diameter to the diameter of the flat basin center was ~5, which is within the upper limit of field-scale examples (Kramer and Shedd, 2017). Thus, average minibasin sidewall slopes were 10%, on the high end of values measured, but within the natural spectrum and below the flow reflection observations of De Falco et al. (2020). The experiments were novel: they accounted for both the 3-D flow and the fact that the adverse slopes were substantially lower than in previous studies (see, e.g., Maharaj, 2012; and Bastianon, 2018), and for the first time modeling was done within the natural parameter space.

The work presented here builds on the study of Reece et al. (2024), who used results from the discharge series to identify and quantify circulation cells aligned with a horizontal plane that were the result of turbidity currents interacting with circular minibasins. Here, variation of the horizontal minibasin aspect ratio is defined by three experiments, with minibasin length-to-width values of 0.5 (short and wide experiment), 1.0 (circular experiment), and 2.0 (long and narrow experiment), which correspond to the 10th, 50th, and 86th percentiles of the Gulf of Mexico depressions measured (Fig. 1C). After carving the minibasins, the deepwater basin was filled with fresh water to an elevation of 0.688 m above the rim of the minibasin.

Experimental slurries were mixed in a set of reservoirs with a combined volume of 3450 L and pumped to a constant head tank before being released into the deepwater basin through a momentum extraction box. The exit point of the box was positioned on the lip of the minibasins, which allowed turbidity currents to immediately descend into the depressions. Turbidity currents were composed of fresh water at room temperature mixed with aluminum oxide beads. Small amounts of calcium carbonate and sodium hexametaphosphate were added to the slurry to limit sediment flocculation (Reece et al., 2024). A point count performed on 100 particles of the sediment with a 100× resolving microscope allowed characterization of the particle size distribution. This resulted in a $D50$ equal to 14 μm, which is only 1 μm more than reported by the sediment manufacturer (Fig. 3). Aluminum oxide has a density, ρ_s, of 3950 kg/m^3. This high sediment density, relative to silica, generates significant excess current density relative to the ambient fluid at low volumetric sediment concentrations (Fukuda et al., 2023). At experimental scale, the greater driving force and low settling velocity of the fine particles supports flow velocity and production of turbulence. These aid suspension of sediment that helps to drive flows into the minibasins with less deposition on the proximal slopes compared to standard quartz slurries. Flows were released into the basin with a volumetric concentration of 0.01, yielding a 2.95% excess density relative to the ambient fluid. Currents had an initial thickness of 37 mm, yielding a ratio of minibasin depth to initial flow height of 3.2. This ratio is poorly defined for field-scale systems and likely varies over several orders of magnitude. However, measurements of feeder channels and minibasin depths from the Brazos-Trinity system, using the Kramer and Shedd (2017) bathymetric map, suggest this ratio is within the distribution of field-scale systems. Input flows had densimetric Froude numbers, Fr_d, of 1.1, where Fr_d is defined as the ratio of advective to gravitational forces within a gravity flow and is equal to

$$Fr_d = \frac{\bar{u}}{\sqrt{RgCH_c}}, \quad (1)$$

where $\bar{u}$ is the depth-averaged flow velocity, R is the submerged specific gravity of sediment, C is the sediment concentration, g is the gravitational acceleration, and H_c is the flow thickness. Hydraulic theory suggests that turbidity currents on slopes >0.5° are supercritical ($Fr_d > 1$; Parker et al., 1987; Wahab et al., 2022). This is supported by flow measurements and/or sedimentary structures from a suite of field-scale systems (Hamilton et al., 2017; Vendettuoli et al., 2019). Proximal slopes of minibasins in the Gulf of Mexico are commonly more than 0.5° (e.g., ~1.7° for Basin II of the Brazos-Trinity system; Kramer and Shedd, 2017), which suggests that input flows are likely critical to slightly supercritical.

Observations in pilot experiments were used to set specific values of input flow discharge, Q_{in}, to facilitate a deliberate transition through the flow-filling (low-flux), striping (mid-flux), and spilling (high-flux) sequence. For each experimental condition, two sustained turbidity currents were released into the basin. The discharge series had Q_{in} equal to 24.0 L/min, 47.7 L/min, and 96.9 L/min, for the low-, mid-, and high-flux experiments, respectively. The duration of each experimental release was 1800 s (30 min). Thus, fluid volumes delivered to experiments, V_{in}, were 720 L, 1431 L, and 2907 L for the low-, mid-, and high-flux experiments, respectively. The input discharges, coupled with a mean flow velocity set by the flow height and Fr_d condition, determined input flow width, yielding flows that were 65 mm, 130 mm, and 260 mm wide for the low-, mid-, and high-flux experiments, respectively. All flows in the aspect ratio series had a Q_{in} of 47.7 L/min (V_{in} for the 30 min flow thus equaled 1431 L) and an input flow width of 130 mm. A summary of important experimental parameters is detailed in Table 1.

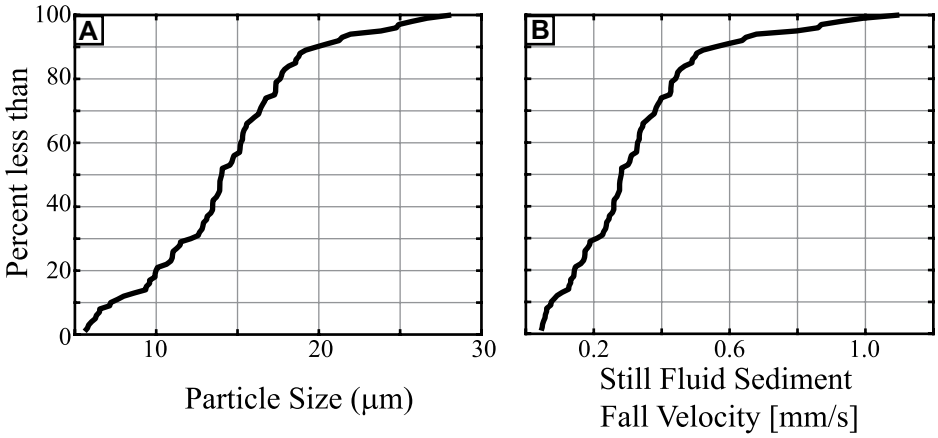

Figure 3. Distributions that describe the size of particles and the corresponding still-fluid fall velocity of sediment introduced into experiments. Still-fluid fall velocity is calculated with the Ferguson and Church (2004) method.

TABLE 1. EXPERIMENTAL PARAMETERS FOR TURBIDITY CURRENTS RELEASED INTO MINIBASINS AND THE GEOMETRY OF MINIBASINS

	Low-flux L = W	Mid-flux L = W	High-flux L = W	Mid-flux L = 2W	Mid-flux L = 0.5W
Input discharge (L/min)	24.0	47.7	96.9	47.7	47.7
Flow width (mm)	65	130	260	130	130
Flow height (mm)	37	37	37	37	37
Sediment concentration	1%	1%	1%	1%	1%
Flow duration (min)	30	30	30	30	30
Flow input volume (L)	720	1431	2907	1431	1431
Basin area (m^2)	7.07	7.07	7.07	7.07	7.07
Basin relief (m)	0.12	0.12	0.12	0.12	0.12
Average basin side wall slope	10%	10%	10%	10%	10%

Experimental Data Collection

Initial basin topography was mapped with a 1 KHz long-range Keyence displacement laser connected to a data logger. This laser was attached to a measurement carriage on top of the deepwater basin and could move in the three Cartesian directions (Fig. 2). This system allows topography to be gathered with a vertical precision of <0.25 mm. Topography was also collected following each flow event, with *x* (downstream) and *y* (cross-stream) node spacing of 5 mm, which allowed the fraction of input sediment trapped in minibasins to be estimated.

Overhead images captured the evolution of the flow field for the duration of each experiment at a frequency of 0.25 Hz (Figs. 4 and 5). To characterize equilibrium conditions, a pulse of red dye was added to the input current at 900 s into each experiment. The volume of the dye was ~250 mL, and the injection duration was ~1–2 s (Fig. 5). Using a technique similar to the Normalized Difference Vegetation Index (NDVI) measurement to identify vegetation in remote-sensing applications (Tucker, 1979; Esposito et al., 2018), we calculated the red color intensity of individual pixels in overhead photos as

$$r^* = \frac{R - B}{R + B}, \quad (2)$$

where *R*, *G*, and *B* are values of the red, green, and blue color bands of an image, which span intensities of 0–255.

Measurements of current velocity were collected using a Nortek Pulse–Coherent Acoustic

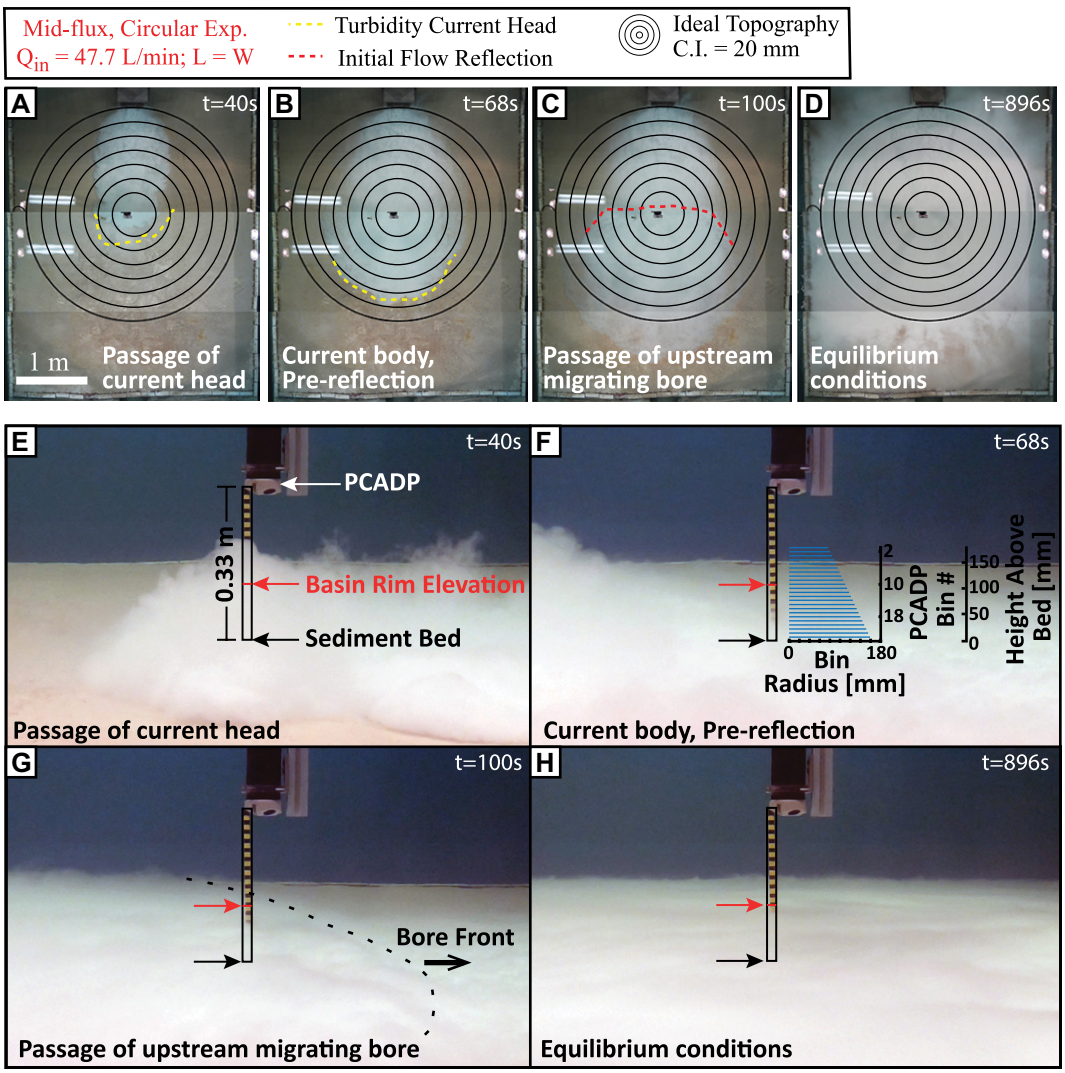

Figure 4. (A–D) Overhead and (E–H) perspective images that document the initial propagation of a turbidity current head (denoted by yellow dashed line) and front of reflected flow (red dashed line) across minibasins, and the equilibrated flow structure. Images are from the mid-flux circular basin condition. Circular solid black lines are ideal contours of topography; the 0.33 m rod used to measure the height of the turbid cloud is outlined in black to aid in comparison between images. Thin horizontal red line over measurement rod denotes elevation of basin rim. Panel F contains plot of radius of Pulse-Coherent Acoustic Doppler Profiler (PCADP) sample volumes with distance from probe.

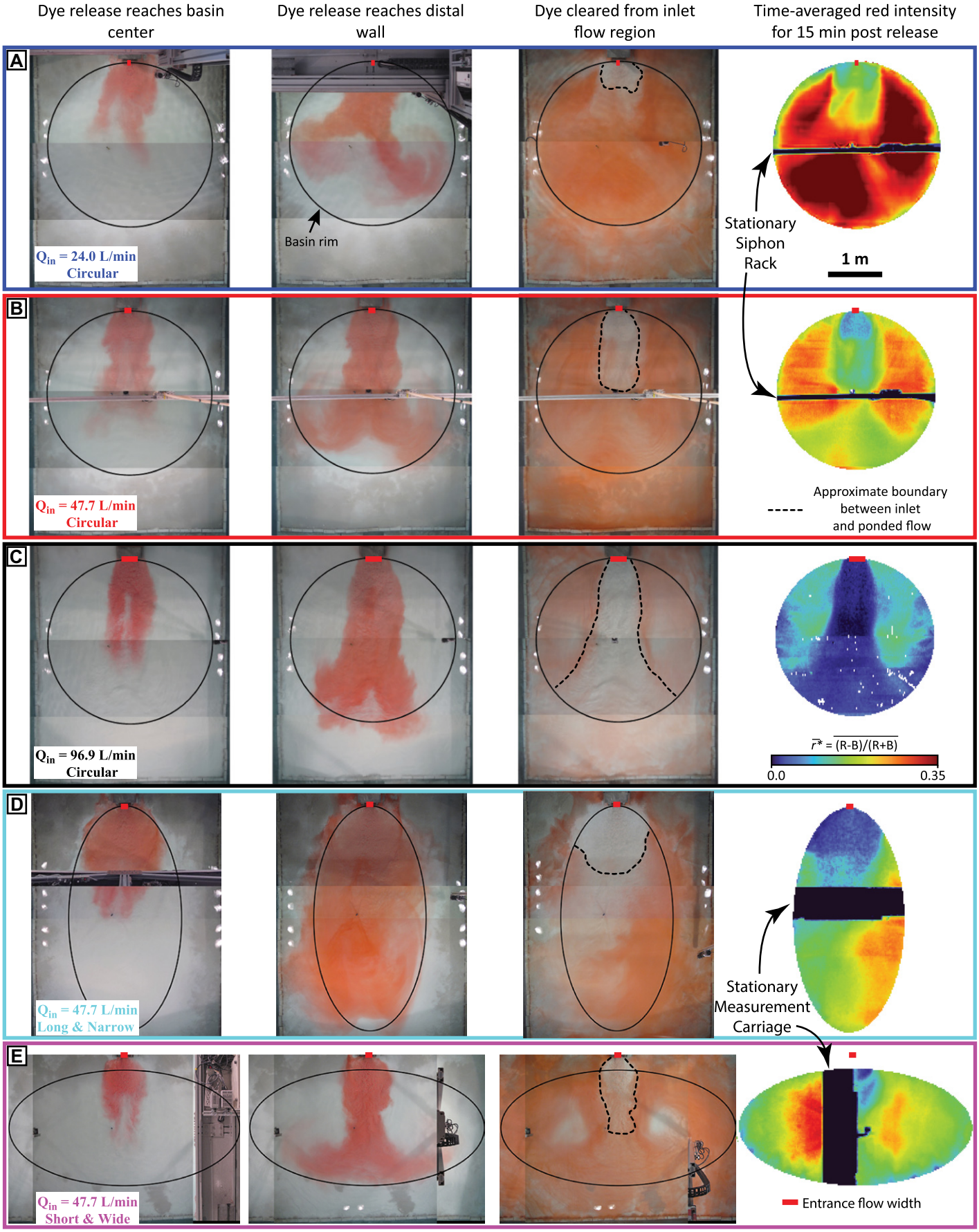

Figure 5. Overhead images and results of image analysis of dye release, in which release occurred at the halfway mark of each experiment to highlight equilibrium conditions. Images capture dye front reaching minibasin center (first column), dye front reaching distal minibasin wall (second column), and dye cleared from inlet flow region (third column), while the red dye intensity temporally averaged over the second half of the experiments is shown in the fourth column. Solid black lines over still images mark the locations of the minibasin rims, and dashed lines approximate the boundaries that separate the inlet from ponded flow. Due to movement of the measurement cart, and placement of the siphon rack, still images do not always come from the same flow events used to measure the average red dye intensity fields.

Doppler Profiler (PCADP) connected to the measurement carriage. This device recorded profiles of the three-component velocity field within 8-mm-tall bins at 1 Hz, which is about one-fifth the initial height of the input flows. The horizontal diameter of the bins varied as a function of distance from the probe, but was 0.21 m at the elevation of the minibasin rim and 0.32 m at the elevation of the minibasin floor (Fig. 4F). Velocity measurements collected with pulse-coherent acoustic doppler profiles have unknown uncertainties (Shcherbina et al., 2018). However, once equilibrium conditions were met within the minibasins, velocity was generally consistent at ±2 mm/s. Some of these oscillations were likely linked to flow turbulence, which suggests a measurement precision of <2 mm/s. Analysis of PCADP data was limited to bins that were fully above the sediment surface. For each experimental condition, the PCADP was positioned over the center of the minibasin for the full duration of the first flow event (flow 1). During the second half of the second flow event (flow 2), the PCADP was deployed to locations on a horizontal grid that covered the river left-hand side of the basin. This grid contained between 27 and 48 nodes, depending on the experiment, and the PCADP was situated over each node for a duration of 25 s.

Measurements of suspended sediment concentrations were collected near the minibasin center during flow 1 of each experimental condition, immediately port-side of the PCADP sample cone. Turbid flow samples came from a set of 10 vertically stacked siphons of 2 mm inner diameter, with 15 mm spacing between siphons and the basal siphon residing 10 mm above the minibasin floor. Approximately 500 mL of turbid flow was extracted with each siphon, from which a measurement of sediment concentration was made by evaporating off the fresh water. Four profiles of concentration were collected for each experiment. Each extraction took 75 s, with collection of each profile beginning 90 s, 210 s, 405 s, and 1560 s into a flow event. The diameter and length of tubing used to extract samples resulted in a lag of 15–25 s between fluid entering and exiting a siphon line.

Finally, to measure the height of the turbid cloud, a stripped vertical rod was placed near the minibasin center, but outside of the PCADP measurement field. Underwater video was collected with a GoPro camera positioned over the river-left moat at a downstream distance aligned with the minibasin center. The center of the field of view was positioned on the measurement rod, with the elevation of the camera just above the minibasin rim. A time series of frames from the GoPro video was used to quantify the height of the turbid cloud using a white color threshold applied over pixels that spanned the measurement rod.

Data Analysis

Time-to-Flow Equilibrium

Motivated by observations in 2-D experiments, Lamb et al. (2004) proposed a method for estimating a setup time for equilibrium conditions in minibasins. This formulation used the time for an upstream-migrating bore to traverse the extent of ponded flow in minibasins. This bore develops due to the reflection of the head of a turbidity current off the distal minibasin slope. The speed of the migrating bore was estimated with the shallow water wave equation:

$$c \cong \sqrt{RgC\Delta H_b}, \tag{3}$$

where ΔH_b is the height of the bore. If one estimates the extent of ponded flow as the full length of the minibasin, L, an equilibrium time, can be estimated as

$$T_b = \frac{L}{c}. \tag{4}$$

While the Lamb et al. (2004) formulation produced a reasonable estimate for 2-D minibasins, there are several simplifications to the formulation. One limiting factor is that it does not account for the time associated with the initial propagation of the current front across the minibasin, T_p, prior to the bore being spawned. This can be estimated as

$$T_p = \frac{L}{u_p}, \tag{5}$$

where u_p is the depth-averaged current velocity in the down-basin direction during the initial flow traverse (i.e., before generation of a bore). Next, theory predicts that upstream turbidity current bore speeds (Bonnecaze et al., 1993) should consider the thickness and velocity of the current during this initial propagation. Here, these are defined as H_p and u_p, respectively, as well as the thickness of the inflated flow post-reflection, H_r

$$c_b = -u_p + \sqrt{RC\frac{g}{2}\frac{H_r}{H_p}\left(H_r + H_p\right)}. \tag{6}$$

The total time necessary for a bore to reach the proximal slope, T, is then:

$$T_{bt} = \frac{L\left(u_p + c_b\right)}{u_p c_b}, \tag{7}$$

which incorporates the time for the flow to traverse the basin and an initial bore to translate upstream. Theoretically, further reflections may occur. However, these are assumed to be negligible in comparison to ambient fluid entrainment and ponded flow dynamics.

A suite of flow observations is used to define the time at which dynamic equilibrium conditions are met in the center of the experimental minibasins (where the greatest density of flow information exists), and these observations are compared to predictions from Equation 7. Equilibrium was assumed once the following three conditions were met. The first condition is that the overhead imagery shows stabilization of the extent of the minibasin filled with turbid fluid, as input flows were balanced by a combination of vertical clear water detrainment, some turbid flow overspilling the full perimeter of the minibasins, and more focused flow overtopping the distal minibasin rims. This is estimated from timeseries of the average white intensity of pixels within a minibasin, as the initial sediment surface was brown, and the sediment introduced into the flows was white. White intensity is calculated as

$$W^* = \frac{R + G + B}{3\left(255\right)}. \tag{8}$$

An error in interpretations of ±20 s is reported, estimated from the 4 s image collection increment and an ambiguity in differentiating characteristics such as turbulence levels, which impact color in individual images. The second condition is that temporal evolution of the turbid cloud height lacks a consistent trend and stabilizes at ±10 mm, the scale of the color alternations on

the measurement rod. The third condition is stabilization of the following three dimensionless numbers that incorporate information from the fluid and sediment transport fields: The first is the ratio of the height of the velocity maximum, H_{umax}, to the depth of the minibasin, D, measured between the basin floor and sill. Low values of this ratio link to conditions with significant flow shear near the bed and vice versa. The second is the bulk Richardson number, Ri_B, which compares forces that promote stable stratification of flows to forces that induce turbulent mixing:

$$Ri_B = \frac{1}{Fr^2} = \frac{RgCH_c}{\overline{u}^2}. \quad (9)$$

Ri_B is calculated using time series of depth-averaged concentration from our siphon system. The third is the Rouse number, p (Rouse, 1939), which characterizes the capacity of currents to suspend sediment and is equal to

$$p = \frac{w_s}{ku^*}, \quad (10)$$

where k is von Kármán's constant (~0.41), and u^* is the shear velocity of the flow. Similar to Altinakar et al. (1996), u^* for turbidity currents was estimated by fitting an equation to our data that describes the logarithmic increase in velocity above a bed, below the velocity maximum, for a shearing flow:

$$u(z) = \frac{u^*}{k} ln\left(\frac{z}{z_0}\right). \quad (11)$$

Specifically, Equation 11 was fit to data from the lowest four velocity bins, which always resided below H_{umax}. The settling velocity, w_s, was calculated for the median particle diameter in the flow using the Ferguson and Church (2004) method.

Strength of Horizontal Circulation

At each site visited by the PCADP during the second half of flow 2, the temporally averaged depth-integrated fluid fluxes in the x (u-velocity component) and y (v-velocity component) directions were calculated, with z as the vertical direction:

$$q_u = \int_0^{H_c} u dz. \quad (12A)$$

$$q_v = \int_0^{H_c} v dz. \quad (12B)$$

Temporal averaging was done over the duration of PCADP sampling at each site. These fields are visualized using vectors that scale with the direction and magnitude of flux. For ease of visual comparison of results from the aspect ratio series, the locations of the measurements were transformed into polar coordinates. A quantitative comparison of experiments was made by calculating the average horizontal flow circulation, Γ. From Stoke's Theorem, horizontal circulation can be calculated as the integral of vorticity within a closed contour. Here, this is calculated for a discrete set of points as

$$\Gamma = \sum_{i=0}^{n} \overline{\Omega_i} A_b, \quad (13)$$

where $\overline{\Omega_i}$ is the vertically averaged flow vorticity at a node, i, calculated from the asymmetric part of the velocity gradient tensor as

$$\Omega = \frac{1}{2}\left[\left(\delta v/\delta x\right) - \left(\delta u/\delta y\right)\right], \quad (14)$$

and A_b is the discrete area associated with a velocity node (x-sample spacing times y-sample spacing). The horizontal circulation is calculated for the closed contour defined by the minibasin bisect line and the river-left rim of the minibasin (i.e., all n nodes that fall within a minibasin). As the sum of the areas of the measurement nodes and the rules used to define the closed contour are the same in all experiments, we can directly compare the strength of circulation induced by the length-to-width ratio of a minibasin.

Sediment-Trapping Capacity

Theory developed by Lamb et al. (2006) predicts the maximum fluid and sediment discharge of currents that deposit 100% of their sediment within a minibasin (i.e., 100% trapping capacity). Currents that deposit all of their sediment within a minibasin detrain their fluid out of the top flow interface. In this framework, the maximum detrainment discharge, $Q_{d,max}$, for a minibasin can be estimated as

$$Q_{d,max} = w_s A, \quad (15)$$

where w_s is the terminal settling velocity of the median particle size in still fluid, and A is the planform area of a minibasin. The discharge series had ratios of $Q_{in}/Q_{d,max}$ of 0.23, 0.47, and 0.95. All flows in the aspect ratio series had $Q_{in}/Q_{d,max}$ equal to 0.47.

Lamb et al. (2006) noted that for natural flows that have a range of grain sizes, the trapping potential of the fine particles in transit will be less than that of the coarse material. Therefore, the Lamb et al. (2006) theory is expanded here to capture how a distribution of grain sizes impacts estimates of sediment-trapping potential. This is accomplished by first comparing how the difference between input current flux and detrainment flux (w_sA) varies over the range of particle diameters introduced into the experiments (Fig. 3). When this number is negative, the ability to detrain flow is greater than the input flux, and as such, a flow comprising that sediment size should be 100% trapped in the minibasin. In contrast, when this number is positive, the influx exceeds the detrainment capacity, and a flow comprising that grain size would partially leak over the minibasin rim. For the distribution introduced into these experiments, the grain size percentile corresponding to the transition between fully trapped and partially leaking flow shrinks as the input flux decreases (Fig. 6A). Application

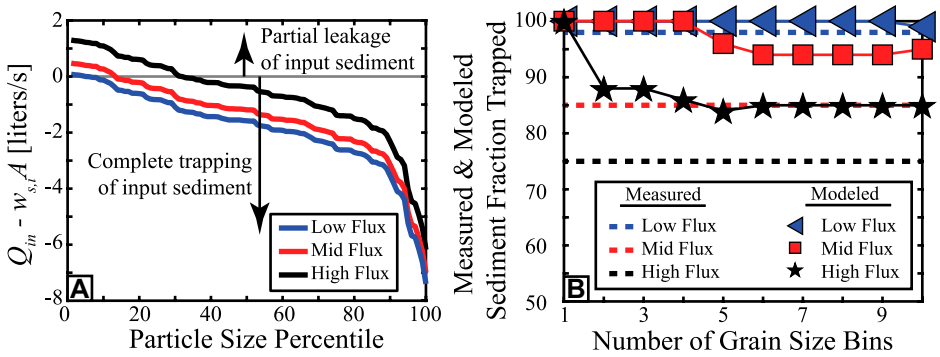

Figure 6. Quantifying the influence of a distribution of particle sizes on the sediment-trapping capacity of the experimental minibasins. (A) Model for each experiment of the expected difference between an input current flux to a basin and the expected detrainment flux for each percentile of the particle size distribution. When this difference is positive, some current and sediment is expected to leak out of the experimental minibasin. (B) Measurements (dashed lines) and models (symbols) of the fraction of sediment introduced to an experiment that gets trapped in the minibasin. Models explore the implications of utilizing information about the grain size distribution when estimating a sediment-trapping fraction through the use of Equation 15.

to the high-flux experiment suggests trapping of 100% of the coarsest 40% of particle sizes, while the low-flux experiment should trap 100% of the coarsest 95% of particle sizes. This is taken one step further to explore how the number of grain-size bins modeled impacts predictions of input sediment-trapped fractions in experiments. This is modeled as

$$F_s = 1 - \left(\frac{1}{NQ_{in}} \sum_{i=1}^{N} \begin{cases} Q_{in} - w_{s,i}A \text{ if } (Q_{in} - w_{s,i}A) \geq 0 \\ 0 \text{ if } (Q_{in} - w_{s,i}A) < 0 \end{cases} \right), \quad (16)$$

where N represents the number of grain size classes modeled. For example, modeling a flow comprising two grain size classes involves the summation of the trapping potential of the 25th and 75th percentile grain diameters, while modeling a flow comprising three grain size classes includes the summation of the trapping potential of the 16th, 50th, and 82nd percentiles, etc. Trapping fractions are calculated by using up to 10 grain size bins, with results generally stabilizing with the use of five or more bins (Fig. 6B). This process predicts trapping potentials of 99%, 95%, and 85% for the low-, mid-, and high-flux experiments, respectively.

Predictions are compared to measurements of trapped sediment. Sequential maps of topography before and after each flow event allow the fraction of sediment trapped in the minibasins to be quantified:

$$F_S = \frac{V_{sediment\ in\ minibasin}}{V_{sediment\ in\ mapped\ region}}. \quad (17)$$

This represents a maximum trapping fraction, as some sediment delivered to the minibasins (flux delivered to the entrance box minus flux to deposition in the entrance box) spilled over the full perimeter of the minibasin rims and ended up in the basin moat.

RESULTS

Observations of Current–Minibasin Interactions

In each experiment, a turbidity current with a pronounced head descended from the entrance box to the minibasin center, which was followed by a thinner current body (Figs. 4, 7, and 8). As the flow fronts traversed the minibasins they widened but did not initially fill the full width of the minibasins (Fig. 4; Videos S1–S5 in the Supplemental Material[1]). Following the runup of distal minibasin slopes, upstream-migrating bores were generated. The tops of these bores were turbulent, mixed with ambient fluid, turbid, and located approximately at the elevation of the minibasin rims. These bores propagated upstream, but also laterally, which widened the flows. After the bores reached the proximal minibasin slopes, the minibasins progressively filled with turbid flow until apparent equilibrium conditions were reached. This took 868 ± 20 s and 596 ± 20 s for the low- and mid-flux experiments, respectively (due to a data collection error, no overhead imagery exists to characterize this time in the high-flux experiment). Overhead images suggest that equilibrium was reached at 476 ± 20 s and 460 ± 20 s for the long and narrow and short and wide experiments, respectively. After these times, the top surfaces of the turbid clouds throughout much of the minibasins were placid, except for a region that extended from the entrance box down

[1]Supplemental Material. Videos S1–S5. Please visit https://doi.org/10.1130/GSAB.S.27335601 to access the supplemental material; contact editing@geosociety.org with any questions.

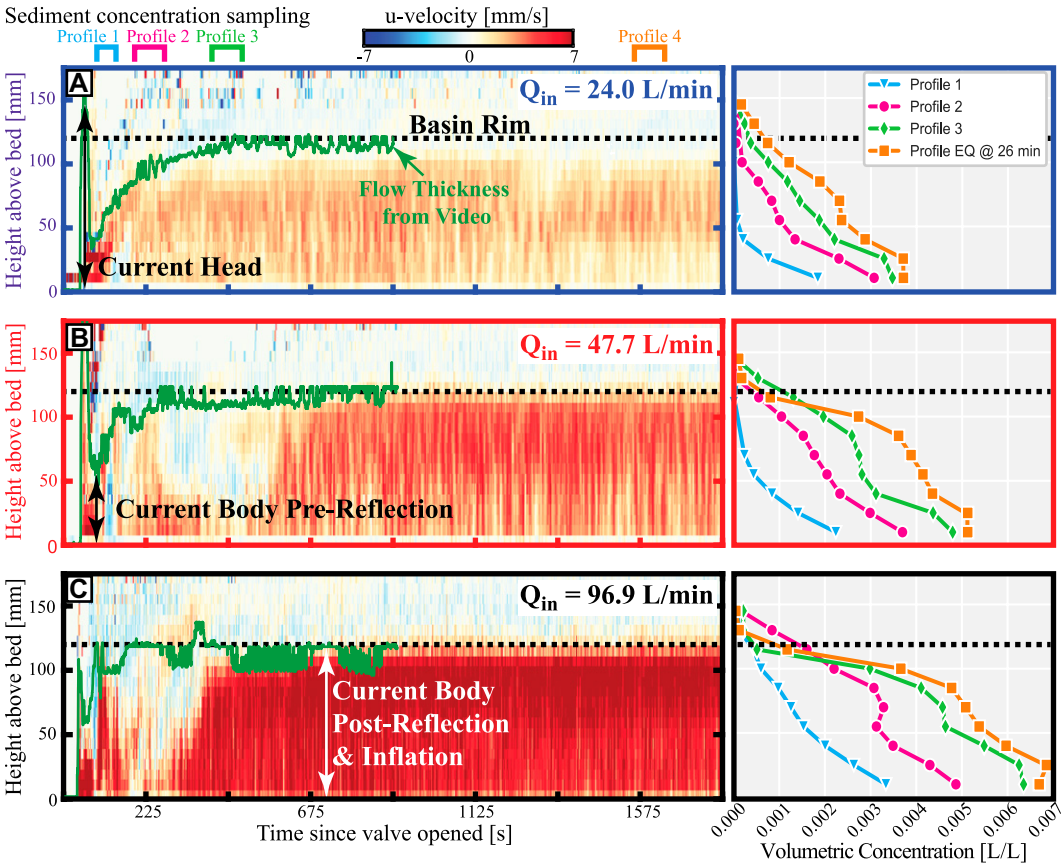

Figure 7. Data used to define the temporally evolving structure of turbidity currents measured at minibasin centers for the discharge series: (A) low-flux condition, (B) mid-flux condition, and (C) high-flux condition. Panels on the left show time series of u-component velocity field measured over minibasin centers. Dashed black lines denote elevation of minibasin rim. Green solid lines show time series of elevation of the top of the turbid cloud, measured from GoPro footage. We limit this elevation time series to the first half of each experiment as dye injection altered parameters used to automate this measurement. Panels on the right show evolving concentration profiles at minibasin centers for four time periods with profile colors that can be linked to times of extraction labeled above the velocity timeseries. Note that the flow took between 15 s and 25 s to pass through siphon lines, which is corrected for here.

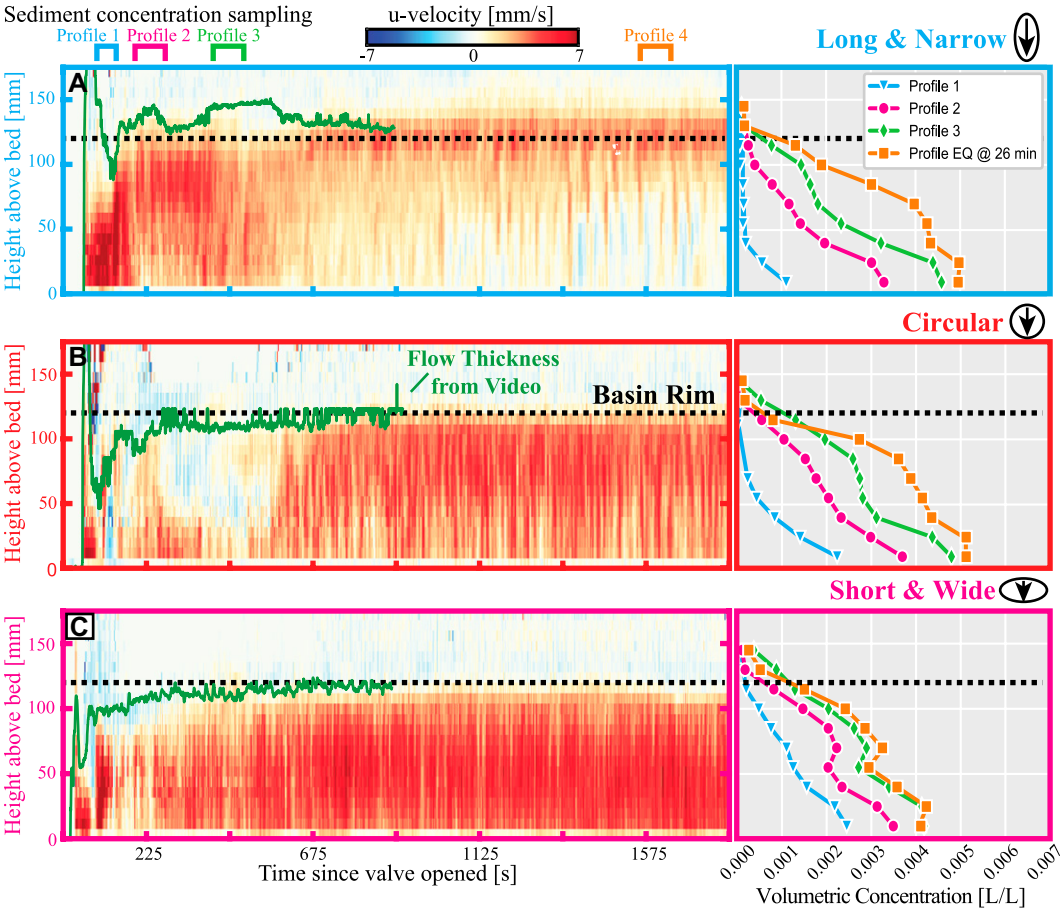

Figure 8. Data used to define the temporally evolving structure of turbidity currents measured at minibasin centers for the planform aspect-ratio series: (A) long and narrow condition, (B) circular condition, and (C) short and wide condition. Panels on the left show time series of u-component velocity field measured over minibasin centers. Dashed black lines denote elevation of minibasin rim. Green solid lines show time series of elevation of the top of the turbid cloud, measured from GoPro footage. Panels on the right show evolving concentration profiles at minibasin centers for four time periods with profile colors that can be linked to times of extraction labeled above the velocity time series. Note that the flow took between 15 s and 25 s to pass through siphon lines, which is corrected for here.

the proximal slopes. These entrance flows had more pronounced turbulent mixing over a distance that scaled with the input flux and inversely with the length-to-width ratio of the minibasins. The terminology of Lamb et al. (2006) is used to separate the turbulent "inlet flow" from the more placid "ponded flow."

Flow Conditions at the Minibasin Center

Next, the temporal evolution of conditions at the minibasin center was characterized with measurements of the turbid cloud height, velocity field, and sediment concentration (Figs. 7 and 8). The temporal evolution of down-basin, u component velocity profiles in all experiments followed a general trend. First, a thick current head was observed, followed by a trailing current body, pre-reflection. Then an arrival of the upstream-migrating bore was observed, which was generally coincident with upstream-directed flow for some period. The location and duration of this return flow varied with Q_{in} and the shape of the minibasin. This was followed by the development of near-equilibrium velocity conditions in most experiments.

In the discharge series, the lowest Q_{in} experiment (Fig. 7A) had the shortest period of upstream-directed flow, which was contained in the lower portions of the flow (bottom 50 mm). Equilibrium velocity conditions appeared to be reached at the minibasin center rapidly during this experiment (~200 ± 30 s). However, oscillations with up-basin flow started to develop at 875 ± 30 s. Note that the associated error (i.e., ± 30 s) is due to ambiguity with interpretations of turbulent flow perturbations observed in all velocity datasets. The mid-flux experiment (Fig. 7B) also had a duration during which return flow was observed low in the flow (100–125 ± 30 s). This was followed by a period characterized by a lower layer of down-system–directed flow and an upper layer characterized by a return flow (250–650 ± 30 s). Velocity conditions stabilized 575 ± 30 s into this experiment. The high-flux experiment (Fig. 7C) had a temporal evolution similar to that of the mid-flux condition. However, return flow was never observed at the base of this flow, and equilibrium conditions were reached 400 ± 30 s into the experiment.

In the aspect ratio series, the long and narrow experiment (Fig. 8A) had no significant upstream-directed flow in its first half. After the propagation of the current head and upstream-migrating bore, a period of high velocities was observed, specifically high in the flow column (225–450 ± 30 s). After this, a gradual evolution of the flow occurred for the remainder of the experiment, with velocities decreasing low in the flow and eventually flipping their orientation, resulting in a weak and pulsing return flow low in the current. Sitting above the return flow was a layer of down-system–directed flow, with peak velocities near the elevation of the minibasin rim. The short and wide experiment (Fig. 8C) was characterized by the propagation of a current head, and—as expected—a short period of body flow before arrival of the migrating bore. This was followed by a period with reduced velocities near the bed and a return flow higher up in the minibasin. Velocity conditions stabilized 400 ± 30 s into this experiment, with down-system flow over the full depth range.

In all experiments, stratified flow was observed with sediment concentration decreasing with distance from the bed. Concentrations increased with time in each experiment, with the largest increase occurring between the first and second measurement periods, which roughly corresponded to before and after the arrival of the upstream-migrating bore. While turbidity currents in all experiments had the same input

concentration, concentrations measured at the minibasin center increased with Q_{in} (Fig. 7). Concentrations were similar in the long and narrow and circular experiments. However, the short and wide experiment had noticeably lower concentrations (Fig. 8). A comparison of profiles at times three (evolving flow) and four (~equilibrium) suggests that time to an equilibrium concentration field decreases with increasing Q_{in} (Fig. 7). Time to an equilibrium concentration field also appeared to decrease as minibasins became short relative to their width (Fig. 8).

Planform Flow Evolution

The fronts of the dyed flows traversed the proximal minibasin slope with minimal widening (Fig. 5; see also Videos S1–S5). With further propagation into the minibasins, a bifurcation of the dye fronts occurred, with some dye eventually routed laterally into twin circulation cells and back to the proximal minibasin slope. The residence time of dye in the inlet flow was noticeably shorter than in the ponded flow. To explore this, the average red color intensity, r^*, of each pixel in the minibasin was calculated for the last 900 s of each experiment. Maps of r^* helped to distinguish the inlet from ponded flow, which were separated by fairly sharp boundaries.

The downstream extent of inlet flow conditions scaled with Q_{in}. For the highest flux condition, the inlet flow extended over the distal minibasin rim (Fig. 5C), which suggests focused discharge of sediment out of the minibasin, Q_{out}. The residence time of flow in the ponded regions appeared to inversely scale with Q_{in}, as the r^* values in the ponded flow decreased with increasing Q_{in}. In the aspect ratio series, the dye front rapidly widened to the full width of the minibasin in the long and narrow experiment. Thus, the full areal extent of the minibasin was filled with red dye upon the front reaching the distal minibasin rim (Fig. 5D). Eventually, red dye was replaced with new white influx sweeping from the proximal to distal regions, and an inlet flow that filled the full lateral extent of the proximal minibasin slope was present. In contrast, the dye front in the short and wide experiment descended into the minibasin with minimal widening before being redirected by the distal slope, which highlighted prominent circulation cells (Fig. 5E). As with the circular minibasins, the r^* map highlights an inlet flow that extended nearly to the minibasin center and strong ponding along lateral minibasin slopes.

Equilibrium Flow Conditions

Values are reported for equilibrium velocity, concentration, and key dimensionless numbers that describe the fluid and sediment transport fields. Measurements were taken 1560–1640 s into each experiment, when the fourth and last concentration profiles were collected. Velocity profiles at the minibasin center were normalized by the maximum value in each profile to aid in comparison. In the discharge series (Fig. 9A), the mid- and high-flux experiments shared similar structures. These flows had a rapid increase in velocity with distance from the bed and then maintained similar values for most of the flow height, but with peak velocities in the upper third of the flow. In contrast, the low-discharge experiment had relatively low velocity in the lower third of the flow. Above this, a pronounced high-velocity region was present in the middle third of the flow, before a decreasing trend in the upper third of the flow. In all experiments, the height of the velocity maximum, relative to the flow height, was elevated in comparison to that of unconfined flows, where the velocity maximum is typically ~30% of the total flow height (Sequeiros et al., 2010). In the aspect ratio series (Fig. 9B), a clear trend was observed with increasing minibasin length to width. The long and narrow experiment had low velocity values with limited structure up to the top third of the flow. Here, velocity values rapidly increased, reaching peak values near the elevation of the minibasin rim. This result is in line with quasi 2-D minibasin studies that report extreme elevation of the u_{max}. For example, a study by Sequeiros et al. (2009) in a pseudo-minibasin that was 9 m long and 0.45 m wide (i.e., $L/W = 20$) had a velocity profile similar to that of the long and narrow experiment reported here. Moving to the circular and then the short and wide experiment, a trend of decreasing height of the velocity maximum and greater shear near the bed was observed.

Next, we present concentration profiles, normalized by the near-bed values, to explore differences in flow stratification (Figs. 9C and 9D).

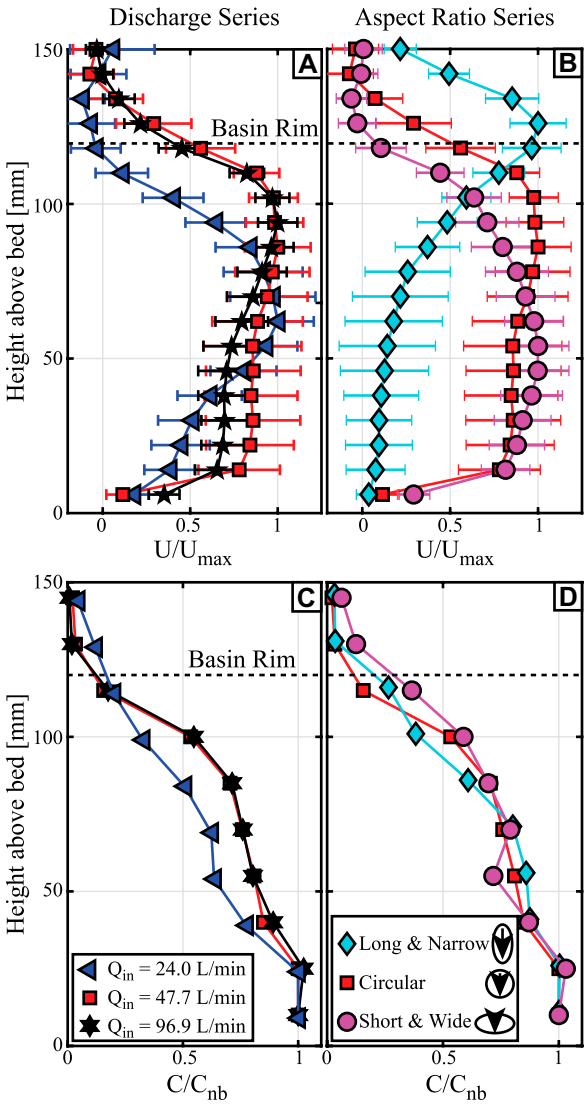

Figure 9. Normalized profiles of (A, B) velocity and (C, D) concentration at equilibrium conditions for (A, C) the discharge series and (B, D) the aspect ratio series. Velocity profiles are normalized by the maximum velocity measured in each profile, while concentrations are normalized by near-bed conditions. Velocity profiles represent temporally averaged conditions for the period over which the fourth concentration profile was extracted (1560–1652 s into each experiment). Concentration profiles come from this same period. Horizontal whiskers around velocity measurements denote the 25th and 75th percentiles of instantaneous velocity measurements during the averaging window. Dashed black lines indicate elevation of minibasin rims.

The normalized concentration structures were remarkably similar in all experiments.

Characterization of Key Dimensionless Numbers

Measurements of the turbid cloud height obtained from analysis of the GoPro footage are similar to the depths of the minibasins, which suggests that H_{umax}/D approximately equals H_{umax}/H_c. However, a portion of the top of the turbid cloud displayed relatively stagnant flow. Given this, the integral length scale is used estimate H_c (Ellison and Turner, 1959):

$$H_c = \frac{\left(\int_0^\infty u dz\right)^2}{\int_0^\infty u^2 dz}. \quad (18)$$

This yielded flow heights similar to, but always less than, minibasin depths (Table 1).

In the discharge series, a complex evolution of H_{umax}/D in the first 400–600 s (Fig. 10) was observed. This included an initial rapid increase in H_{umax}/D to values of between 0.5 and 0.9, followed by a period where peak velocity elevations fell to 0.2–0.5 of D. After this, H_{umax} again increased and equilibrated at values ranging between 0.5 and 0.8 of D. Evolution of H_{umax}/D was more complex in the aspect ratio series. The long and narrow experiment had an increase in H_{umax}/D over the first 380 s to a value of ~0.7. Between 380 s and 580 s, H_{umax}/D dropped and oscillated between 0.4 and 0.7, and then rapidly increased to a value >1 for the remainder of the experiment. In contrast, H_{umax}/D rapidly increased in the first 200 s of the short and wide experiment before stabilizing at ~0.5.

In all experiments, the current body pre-reflection had Ri_B of <1, which corresponds to supercritical Fr_D (Fig. 10). For the discharge series, Ri_B rapidly climbed after the arrival of the upstream-migrating bore and then settled to near-equilibrium values after ~600 ± 30 s. A similar evolution of Ri_B was observed in the short and wide experiment. The evolution of Ri_B in the long and narrow experiment was more complex specifically due to the development of return flow in the second half of the experiment that resulted in unstable Ri_B, through singularities in Equation 9 when $\overline{u} \to 0$. Spatially across the minibasin depth, average velocities may tend to be zero due to return flow. However, except at layer interfaces or velocity maximum, velocity magnitude and critically shear across-the-water column depth is nonzero, and even if $\overline{u} = 0$, the flow may be unstable. Further work considering internal flow stability and turbulent mixing processes within these 3-D flows may consider the ratio of local stratification to shear, through the gradient Richardson number (see, e.g., Dorrell et al., 2016).

In the discharge series, p values rapidly stabilized just below 10^{-1} for the mid- and high-flux conditions (Fig. 10). While the first half of the low-flux condition followed a similar evolution, the second half of the experiment was characterized by oscillation in p with peaks of up to ~0.7, which suggests a transition to sediment being transported lower in the flow. In the aspect ratio series, the short and wide experiment followed a trend similar to those of the high- and mid-flux experiments. However, the long and narrow experiment displayed oscillations in p beginning ~600 s into the experiment. Oscillations strengthened as this experiment progressed, reaching values >1.

Dimensionless numbers that characterize the equilibrium fluid and sediment transport fields showed clear gradients as a function of Q_{in} and minibasin length to width. The height of the velocity maximum, relative to the minibasin depth, systematically increased as a function of Q_{in} and the length to width of the minibasins (Fig. 11A), which suggests a systematic change in the shear profile near the bed. Bulk Richardson numbers indicated that the strength of stratification relative to turbulent mixing decreased as minibasin influx increased. In the aspect ratio series, Ri_B values showed a strong positive correlation with minibasin length to width, with extreme suppression of mixing in the long and narrow experiment (Fig. 11B). With regard to sediment suspension capacity as measured through p, we note nonlinear trends as a function of Q_{in} and minibasin length to width. The low-discharge and long and narrow experiments had p values above 0.2, which suggests the loss of suspension capacity, while all other experiments had similar p values that were <0.07 (Fig. 11C).

Minibasin-Wide Flow Structure

As first highlighted in a study by Reece et al. (2024), circulation cells were observed with flow moving up distal minibasin slopes that was directed laterally away from the minibasin bisect line. Minibasin slopes continued to affect the flow direction, resulting in circulation cells that included up-system–directed flow along a portion of the lateral minibasin slopes. The center of these cells was laterally offset from the minibasin center. When normalized by input flux, the shape of the circulation cells across the discharge series was remarkably similar in all experiments (Fig. 12A). Viewing the flow field

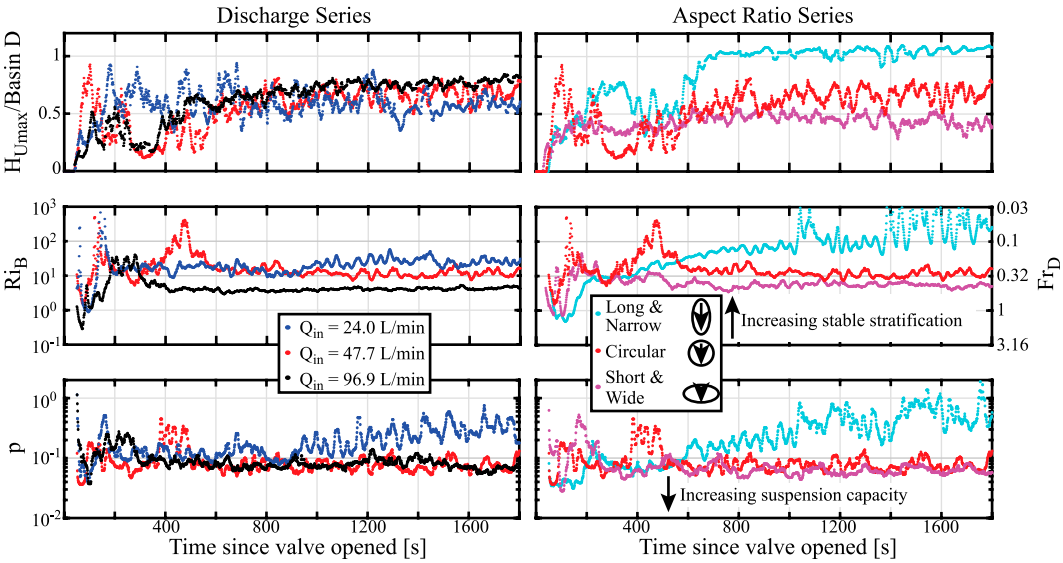

Figure 10. Time series of dimensionless numbers that quantify the evolving fluid and sediment transport fields in the discharge series (left column) and aspect ratio series (right column). Top row details the height of the velocity maximum relative to basin depth, the middle row details the Bulk Richardson number that quantifies stratification of flow relative to shear, and the lower row details the Rouse number that quantifies the suspension capacity of the flows.

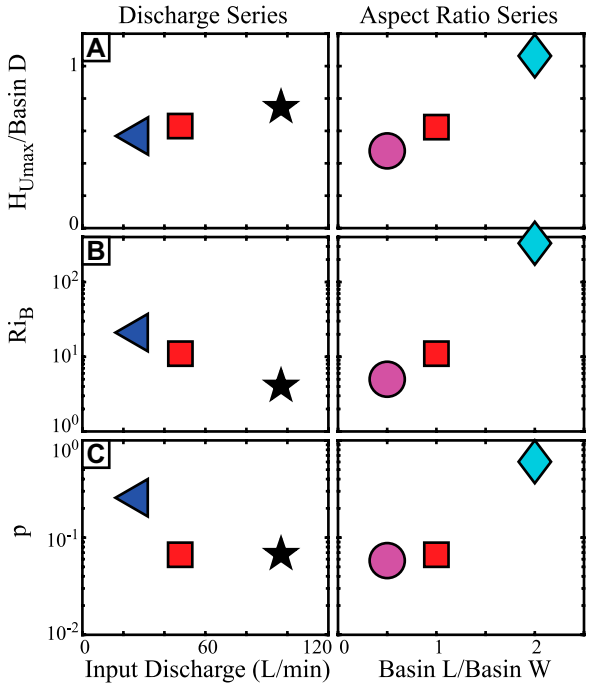

Figure 11. Temporally averaged values of dimensionless numbers that quantify the equilibrium fluid and sediment transport fields in the discharge series (left column) and aspect ratio series (right column). Averaging was done over the time when the fourth concentration profile was extracted (1560–1652 s into each experiment).

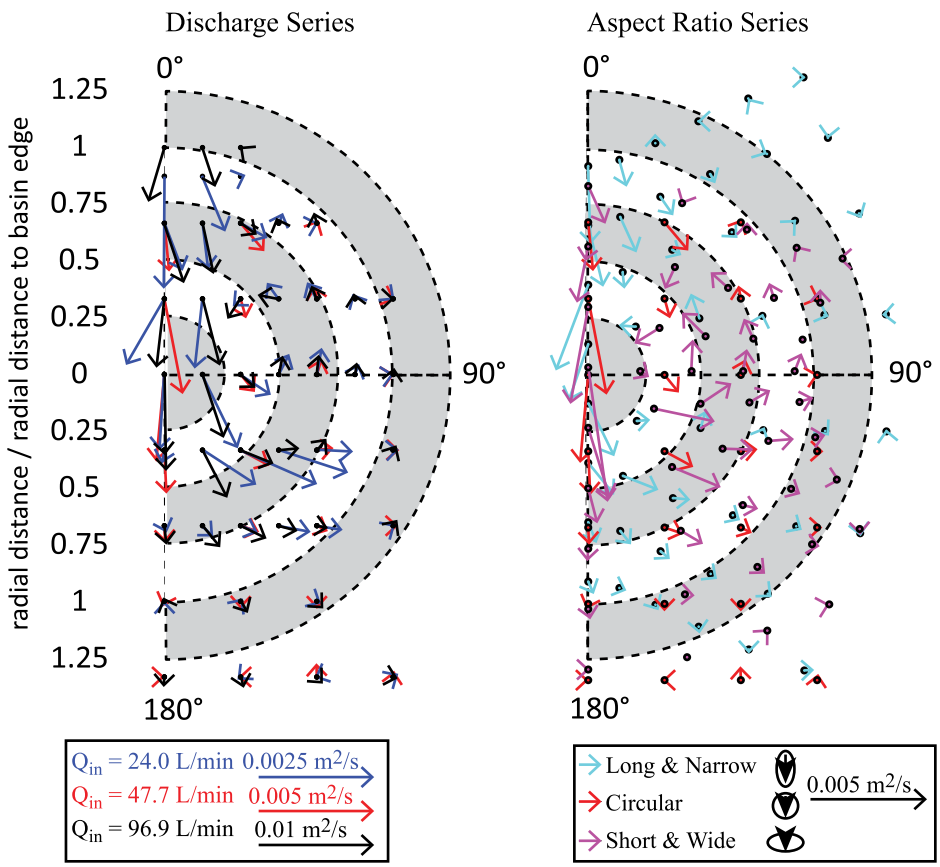

Figure 12. Map of vector field that quantifies the depth integrated *u* (down-basin) and *v* (cross-basin) velocity components for each experimental condition placed into a polar coordinate system. Note the differences in the scaling of quivers in the discharge series, which aids in the comparison of velocity field structures between conditions.

in polar coordinates for the aspect series reveals that the magnitude of current flux in the circulation cells was generally higher in the short and wide experiment, compared to the long and narrow experiment (Fig. 12B). The circulations of the long and narrow and short and wide experiments were 0.0027 m²/s and 0.0043 m²/s, respectively.

Minibasin Sediment-Trapping Capacity

The first experiment performed was the high-flux circular condition, designed with a sediment input flux nearly equal to the sediment-trapping potential. This was calculated with the equation proposed by Lamb et al. (2006), Equation 15. However, results suggest that, at most, 75% of the sediment input in this experiment was trapped in the minibasin. Estimates for the sediment fractions trapped in the mid- and low-flux experiments were 85% and 98%, respectively (Figs. 13 and 14). Thus, near-complete sediment trapping did not occur until the flow influx dropped to approximately one-quarter of that proposed by the earlier theory. The elongated minibasins have sediment-trapping fractions within a percent of the mid-flux circular case, which suggests that minibasin planar geometry does not strongly influence sediment-trapping potential (Figs. 13 and 14).

DISCUSSION

Time to Equilibrium Flow Conditions in Minibasins

The time necessary for flow properties to stabilize in minibasins has implications for the structure of minibasin-filling turbidites. When turbidity currents require significant time to reach equilibrium in minibasins, turbidities record flow development in their lamination and sedimentary structures. In contrast, flows that rapidly reach equilibrium should deposit relatively homogeneous beds.

Here, the theory that time-to-flow equilibrium equals that for a migrating bore to traverse the extent of ponded flow in minibasins is tested, with a focus on the circular mid-flux condition. Overhead imagery is used to estimate the time into this experiment when the migrating bore, spawned from runup of the distal slope, reaches the proximal rim: 200 ± 20 s. The Lamb et al. (2004) formulation, specifically Equations 3 and 4, is applied to estimate this time, using a range of plausible ΔH_b measured from the GoPro footage (0.01–0.02 m) and C measurements from the first profile of the experiment (C = 0.001–0.002). This yields an estimate for the bore to reach the proximal slope of 124–212 s. However, at this

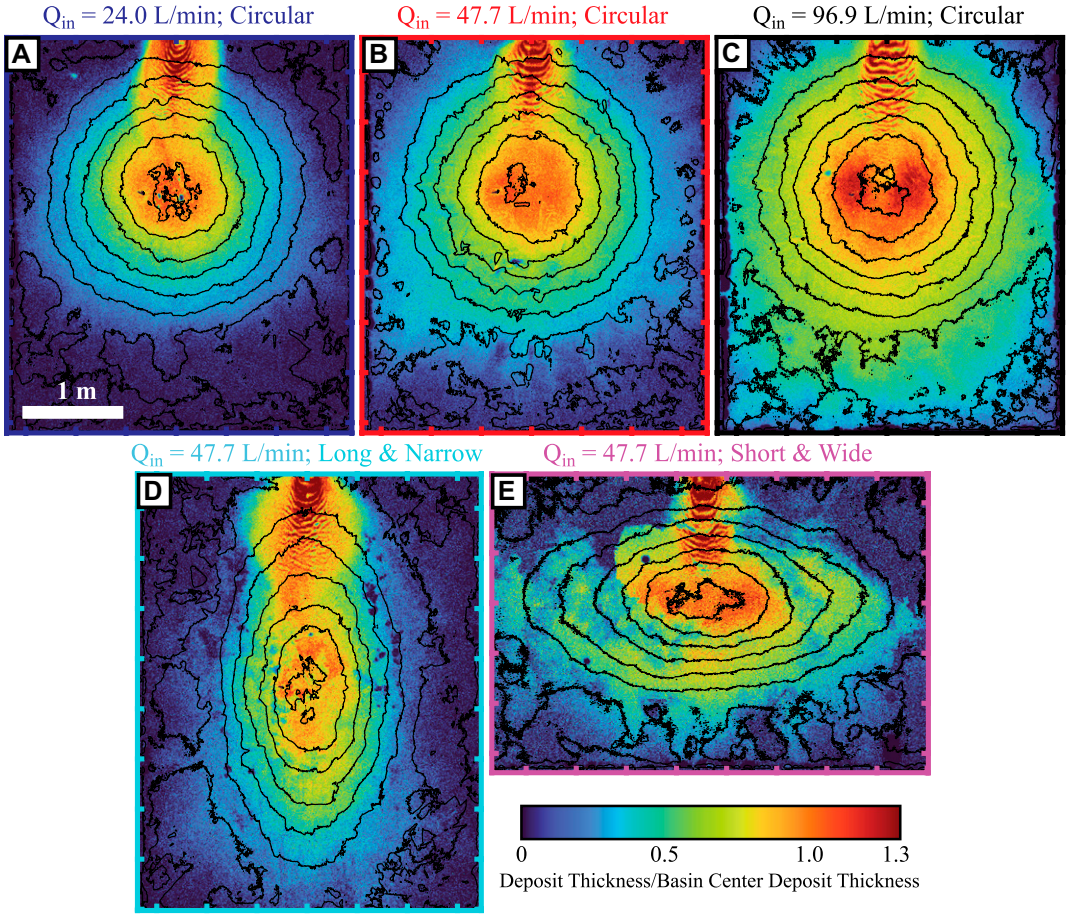

Figure 13. Isopach maps for the (A–C) discharge series and (B, D, and E) aspect series. Maps of deposition are the result of two flow events released into each minibasin. Contour lines define the initial topography of each experiment with a contour interval of 20 mm increasing from the minibasin center elevation. Isopach maps are normalized by deposit thickness at minibasin centers to aid in the comparison.

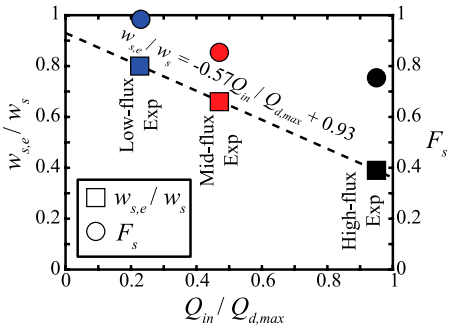

Figure 14. Ratio of effective to still-fluid fall velocity of sediment and the fraction of sediment trapped in discharge series experiments as a function of the input flux to an experiment normalized by the theoretical detrainment flux of a minibasin following Lamb et al. (2006). Dashed line represents best-fit trend line of $w_{s,e}/w_s$ as a function of $Q_{in}/Q_{d,max}$.

time, the concentration field was not equilibrated, nor was the velocity field (Fig. 7). The second concentration profile (210–285 s) was significantly different from the third (405–480 s). Including the time for the initial propagation of the current front across the minibasin, Equation 5, and the more advanced Bonnecaze et al. (1993) formulation, Equation 6, for the bore speed yields an updated estimate for the time necessary for equilibrium to be reached of 182 s. This time reasonably matches observations from overhead imagery for when the bore reached the proximal rim of the minibasin (200 ± 20 s), but it still does not match the time when equilibrium fluid and sediment transport parameters were reached (Ri_B stabilized at ~575 ± 30 s).

The difference between the Lamb et al. (2004) theory and the observations at the center of the minibasin from this study are explained here as a result of laterally evolving concentration and velocity fields, which result in laterally evolving pressure gradients. Recasting the problem to consider these observations, the time to equilibrium is hypothesized to scale with the time to replace ambient fluid in minibasins with turbid flow. For a condition in which the height of the ponded cloud is equal to the minibasin depth, this filling time is

$$T_f = \frac{V_b}{(Q_{in} F_s)}. \quad (19)$$

Note that the influx is multiplied by the fraction of sediment trapped in the minibasin (F_s), which is assumed to be equal to the fraction of flow trapped in the minibasins (F_T), to account for flux that does not aid in the replacement of ambient fluid. Applying Equation 19 to the mid-flux condition yields a T_f of 521 s, similar to the time at which fluid and sediment transport conditions are reached.

As minibasin volume, V_b, F_s, and Q_{in} are identical in the aspect ratio series, estimates of T_f are identical. However, quasi-equilibrium conditions were not reached until ~675 s into the long and narrow experiment (when H_{umax}/D stabilizes) and 400 s into the short and wide experiment (also when H_{umax}/D stabilizes). This suggests a secondary control on time to equilibrium that correlates with the planform aspect ratio. Results from the discharge series also support the use of Equation 19 for predicting time-to-flow equilibrium. T_f is predicted at 875 s and 219 s for the low- and high-flux conditions, respectively. Results from the low-flux experiment are interpreted to reach equilibrium at ~875 s when periodic oscillations in Ri_B and p develop. Support for this interpretation, over an earlier time, is found in the evolving concentration profiles dur-

ing the first 500 s of this experiment, and in the time necessary for the white color intensity over the minibasin to equilibrate. Results from the high-flux condition reach equilibrium at ~400 s when the depth-averaged velocity stabilizes. Taken as a whole, the minibasin filling time, T_f, better scales with the time to equilibrium conditions compared with the bore migration time, T_b, proposed by Lamb et al. (2004), but further work could better quantify secondary influences.

Prediction of Time to Equilibrium in Field-Scale Minibasins

Here, the time necessary for turbidity currents entering minibasins to reach flow equilibrium, based on fluid replacement (Equation 19), is explored for field-scale minibasins and compared to observations and predictions of the duration of sustained field-scale flows. This analysis focuses on the Brazos-Trinity system of linked minibasins, given the wealth of published data on their geometry and stratigraphy, specifically for Basins II and IV (Fig. 1; Pirmez et al., 2012; Prather et al., 2012). An assumption of Fr_D critical conditions entering each minibasin, feeder channel/canyon widths and depths, and a range of concentration values (1%–5%) are used to estimate Q_{in}. Minibasin volumes, for conditions that precede the last episode of significant sediment delivery (24.3–15.3 ka), are estimated with the minibasin dimensions reported in Pirmez et al. (2012) for estimating T_f. This yields values of 1–2 days and 5–10 days for Basins II and IV, respectively. Notably, turbidites in Basin IV do not onlap high onto minibasin slopes, which suggests the volumes of equilibrated turbid clouds were significantly less than if they had been estimated from the rim elevation. This would mean the filling times were shorter than those estimated above. Regardless, these estimates are significantly longer than the ~1 h suggested by Lamb et al. (2004) through application of Equations 3 and 4 to these same minibasins. Measured (Xu et al., 2004; Azpiroz-Zabala et al., 2017; Talling et al., 2022) and estimated flow durations (Jobe et al., 2018) in nature rarely exceed 10 days, and are more commonly less than a day, which suggests that a significant percentage of the active flow time in these minibasins was associated with unsteady/evolving flow. Under nonequilibrium flow conditions, a more heterogenous structure of minibasin-filling turbidites may be speculated, attributable to variations in shear velocity, sediment suspension, and transport during flow evolution. However, further work should evaluate the importance of the ratio of feeder channel depth to basin depth, and flow duration to ponding time, to test if there are pseudo-steady states of inflation to equilibrium.

Three-Dimensional Structure of Inlet and Ponded Flow

Overhead imagery of the propagation of the head of turbidity currents entering the experimental minibasins captures the initial lateral structure of turbidity currents (Fig. 4; Videos S1–S5). The structure of the inlet flow is later captured with imagery of the dye release (Fig. 5) and with the minibasin-wide velocity field map (Fig. 12), during equilibrium conditions. It is highlighted that for all conditions, except the long and narrow experiment, the initial flow traverse and structure of the dye front indicate that the inlet flow did not widen to fill the full lateral extent of the minibasins. Rather, maps of the average red intensity measured over the second half of the experiments have sharp gradients between regions of low and high r^* that are interpreted as boundaries between inlet and ponded flow conditions. The sharp gradients separating these regions suggest sharp shear boundaries with limited mixing across the boundaries (Fig. 5). Higher velocities and turbulent mixing in the inlet flow likely led to greater bed reworking in these regions, relative to the portions of the minibasins covered with ponded flow. This is supported by the fields of ripples that developed on the proximal slopes (Fig. 13). For field-scale flows, this enhanced bed reworking could lead to channelization, which is seen in the Brazos-Trinity basins (Prather et al., 2012) and other minibasins across the Gulf of Mexico (Kramer and Shedd, 2017).

The extent to which inlet flow conditions penetrated minibasins likely has implications for interpretations of the time to equilibrium. Most of the observations used to define when equilibrium is reached come from the minibasin center. Notably, the low-flux experiment and long and narrow experiment, which had equilibrium times that were difficult to interpret, had inlet regions that did not extend to the centers of the minibasins. Uncertainty in the timing of equilibrium conditions is likely set by the downstream circulation cell. Specifically for the long and narrow experiment, the low lateral circulation allows the penetration of an up-basin flow near the bed. However, this vertical circulation was not strong or stable, and thus resulted in pulsing up-basin flow.

Given that the inlet flow failed to expand to the full minibasin width in the experiments described here, except for the long and narrow experiment, the circulation cells (Fig. 12) were critical for distributing sediment throughout the minibasins. Velocity magnitude in the experimental cells was significantly less than in the inlet flow but sufficient to result in deposits that evenly blanketed the lateral slopes (Figs. 13). Similar depositional patterns as those seen in the experiments described here are seen in field-scale systems, including turbidites that blanket the full width of minibasin floors and onlap sidewalls (Prather et al., 2012). While the strength of circulation scaled with input discharge (Figs. 12A), it also inversely scaled with the length-to-width ratio of minibasins. In the short and wide experiment, the average horizontal circulation, calculated with Equation 13, was 59% greater than that of the long and narrow experiment, even though their input discharges were identical. As the lateral circulation is reduced in the long and narrow minibasin, stagnant or weakly pulsing upstream-directed flow developed low in this minibasin. Thus, near-bed shear stress was reduced. This forced newly introduced flow to move at the elevation of the minibasin rim. However, as flow propagated across this minibasin, sediment continuously fell into the lower stagnant flow and then toward the bed. The low near-bed shear stress meant that sediment was unlikely to get resuspended. Similar mechanics in long but narrow field-scale minibasins would likely produce more homogenous turbidites compared to short and wide basins.

General Implications for Field-Scale Flow Obstacles

The dynamics of the interactions between turbidity currents and topography reported here have implications beyond enclosed minibasins. A key observation from our work is the dramatic alteration of the vertical flow structure, relative to unconfined flows, which results from flows hitting a topographic obstacle (Figs. 7 and 8). In general, this results in elevating the u_{max} flow height (Fig. 11) and less near-bed shear stress. The magnitude of this u_{max} height increase, relative to unconfined conditions, is controlled by input discharge and the minibasin planform aspect ratio. The effect due to minibasin aspect ratio appears to be significant and is perhaps unintuitive. Flows in our long and narrow minibasin had u_{max} elevations at the minibasin rim and pulsing return flow near the bed during equilibrium conditions due to suppressed horizontal circulation relative to circular depressions. This aspect ratio represents the 86th percentile of minibasin length to width, and thus, it is well within the natural spectrum.

Beyond minibasins, it is anticipated that a similar enhanced elevation of u_{max} could result from flows hitting obstacles such as landslide dams in submarine channels, like those recently documented in the Congo submarine channel (Pope et al., 2022b). While the elevation of u_{max} should reduce near-bed shear stresses in the ponded flow behind the dams, it may result in especially high shear stresses over the dam sill point, as u_{max}

could reside at or above the spill elevation of a dam, much like in the long and narrow experiment. This could aid in the erosion of landslide dams, thus reducing the time during which particulate organic carbon and other clastic particles are sequestered. For large landslide dams, with sills at the elevation of a canyon or channel rim, an elevated high-velocity core could increase the shear stress on canyon or channel walls and enhance the likelihood of avulsions. In contrast, the short and wide experiment had a flow structure that most resembled unconfined flows. This suggests that flows hitting obstacles that lack lateral confinement (e.g., shale ridges) may experience less dramatic alteration of their flow structure than ponded flows constrained by sidewalls that reduce lateral circulation. This should allow flows to maintain relatively high near-bed shear stresses in regions up dip of these obstacles.

Minibasin Sediment-Trapping Potential

Theory emanating from earlier 2-D experiments on turbidity current–minibasin interactions suggested that the trapping potential of flows entering minibasins could be estimated with Equation 15 (Lamb et al., 2006; Toniolo et al., 2006a). Application of this theory to the experiments described here yields ratios of minibasin inlet to detrainment fluxes of between 0.95 and 0.23 for all experiments. As such, all experiments should have trapped 100% of the sediment that entered the minibasins. Accounting for the distribution of grain sizes introduced to minibasins lowers trapping predictions to 85%–99% (Fig. 6), which is still significantly higher than the estimates of sediment trapping from the repeat bathymetric surveys reported here (Figs. 13 and 14). It is emphasized that the trapping fractions reported here are likely overestimates due to loss of sediment out of the mapped region, which would only expand this discrepancy.

Here, the discrepancy between modeled and measured trapping fractions is suggested to arise due to a reduction in the effective sediment fall velocity from the still-fluid fall velocity by the detrainment flux. For example, each of the experiments evolved to an equilibrium condition in which the full area of a minibasin was covered by turbid flow. Multiplying the basin area by the sediment fall velocity results in a predicted vertical detrainment velocity, w_d, equal to $-w_s$. This can be used to estimate an effective fall velocity, $w_{s,e}$, as

$$w_{s,e} = w_s + w_d. \quad (20)$$

In the scenario above, the still-fluid sediment fall velocity exactly balances the detrainment velocity, and particles cease to fall. However, this would shut down the detrainment flux, and the particles would start accelerating to their terminal velocity again. Ultimately, a balance between a detrainment flux and the still-fluid sediment settling velocity such that $w_s >> w_{s,e} >> 0$ is envisioned. This balance is estimated for the circular experiments in the following manner. First, an equilibrium detrainment flux is estimated to be equal to the input flux multiplied by the fraction of flow trapped in a minibasin. For simplicity, the flow-trapping fraction is assumed to be equal to the sediment-trapping fraction. As such, fluid that is not lost to focused sediment-charged overspill must be detrained from the flow's top surface. A vertical detrainment velocity is calculated by dividing the detrainment flux by the minibasin area. Using these estimates with the still-fluid sediment settling velocity of the D_{50} introduced into the experiments and Equation 20 yields $w_{s,e}$ of 0.22 mm/s, 0.18 mm/s, and 0.11 mm/s in the low-, mid-, and high-flux experiments, respectively. Dividing each $w_{s,e}$ by w_s allows one to find the relative reduction in sediment fall velocity due to fluid detrainment, which equals 0.80, 0.66, and 0.39 for the low-, mid-, and high-flux experiments, respectively. The key finding here is that the detrainment flux influences the ability of particles to fall to the bed, and as such reduces the sediment-trapping potential of minibasins. This reduction in $w_{s,e}$ from w_s is dependent on the input flux, with higher input fluxes having a greater reduction in fall velocity due to greater detrainment. This reduction is not trivial. The high-flux experiment was designed to capture all input sediment but likely suffered a reduction in fall velocity of >50% due to fluid detrainment. Extrapolation of a linear trend fit to estimates of $w_{s,e}/w_s$ as a function of $Q_{in}/Q_{d,max}$ (Fig. 14), while acknowledging the limited number of experiments performed, is internally consistent, as a zero influx would result in an effective fall velocity equal to the still-fluid fall velocity. Ultimately, these results suggest that predicting the trapping potential of minibasins with high precision requires modeling of multiple grain size classes and accounting for the reduction in effective fall velocity due to fluid detrainment. This suggests that minibasins are not as effective at trapping sediment as predicted in prior work (Lamb et al., 2006; Toniolo et al., 2006a), specifically for fine and light particles, such as particulate organic carbon. These results suggest low trapping of organic carbon in proximal minibasins, relative to coarser clastic particulates. Organic carbon expelled from proximal depressions will be caught by distal depressions, resulting in a down margin gradient in turbidite TOC.

CONCLUSIONS

Turbidity currents flowing down continental margins often encounter complex topography, including enclosed depressions termed minibasins. While prior studies used physical experiments to examine how turbidity currents interact with 2-D minibasins, little is known about these interactions in 3-D settings. For the first time, experimental turbidity current interactions have been quantified across a range of 3-D minibasins designed with geometries that scale to real-world geological features. This suite of experiments demonstrates the influence of input flow discharge and minibasin shape on the evolving 3-D flow field and the capacity of minibasins to induce sedimentation. The key findings include the following:

(1) The time necessary for flows to approach equilibrium conditions is equal to the volume of ponded flow divided by the input flow discharge. Application to the characteristic Brazos-Trinity minibasin system of the Gulf of Mexico suggests that flows may often need several days to equilibrate, and that the texture of basin-filling turbidites may be dominated by flow conditions that evolve with time. As such, structureless minibasin-filling turbidites will be rare and linked to infrequent and long-duration events.

(2) The shape of minibasins has a strong control on the 3-D dynamics of ponded turbidity currents. In all experiments, the development of horizontal circulation cells that distribute fluid and sediment throughout minibasins was observed. Critically, the ability of currents to circulate along a horizontal plane is reduced as minibasins become 2-D, for example, long relative to their width. This reduces flow velocities near the bed and can even result in weak upbasin, near-bed flow in long but narrow minibasins. An associated reduction in near-bed shear stresses further influences the degree of heterogeneity in minibasin-filling turbidites.

(3) The experiments reported here were designed to trap the experimental flows and all of their suspended sediment. This design utilized theory developed from observations of 2-D experiments that equated minibasin trapping potential to the product of minibasin area and the still-fluid fall velocity of the suspended sediment. However, significant stripping of flow and sediment was observed in all but our lowest influx condition. This is attributed to differences in trapping potential over a distribution of particle sizes introduced to a basin and a reduction in effective sediment fall velocity from the fluid that vertically detrains from minibasins. Reduction in trapping potential will be greatest for small and low-density particles, for example, particulate organic carbon and microplastics.

ACKNOWLEDGMENTS

This project was supported by student grants to J.K. Reece from the Geological Society of America, the American Association of Petroleum Geology, and SEPM (Society for Sedimentary Geology), and faculty grants to K.M. Straub from the Tulane Carol Lavin Bernick Fund, ExxonMobil, and the U.S.-Israel Energy Center funded through the Binational Industry Research and Development Foundation. R.M. Dorrell was funded by the Natural Environment Research Council NE/S014535/1. We thank associate editor Alex Whittaker and Gareth Keevil for reviews that significantly improved the manuscript.

REFERENCES CITED

Alexander, L.L., and Flemings, P.B., 1995, Geologic evolution of a Pliocene–Pleistocene salt-withdrawal minibasin: Eugene Island Block 330, offshore Louisiana: AAPG Bulletin, v. 79, no. 12, p. 1737–1756.

Altinakar, M.S., Graf, W.H., and Hopfinger, E.J., 1996, Flow structure in turbidity currents: Journal of Hydraulic Research, v. 34, p. 713–718, https://doi.org/10.1080/00221689609498467.

Andresen, K.J., Huuse, M., Schødt, N.H., Clausen, L.F., and Seidler, L., 2011, Hydrocarbon plumbing systems of salt minibasins offshore Angola revealed by three-dimensional seismic analysis: AAPG Bulletin, v. 95, no. 6, p. 1039–1065, https://doi.org/10.1306/12131010046.

Azpiroz-Zabala, M., Cartigny, M.J., Talling, P.J., Parsons, D.R., Sumner, E.J., Clare, M.A., Simmons, S.M., Cooper, C., and Pope, E.L., 2017, Newly recognized turbidity current structure can explain prolonged flushing of submarine canyons: Science Advances, v. 3, no. 10, https://doi.org/10.1126/sciadv.1700200.

Badalini, G., Kneller, B., and Winker, C.D., 2000, Architecture and processes in the late Pleistocene Brazos-Trinity turbidite system, Gulf of Mexico continental slope, *in* Weimer, P., ed., Deep-Water Reservoirs of the World: Gulf Coast Section SEPM (Society for Sedimentary Geology) Foundation 20th Annual Bob F. Perkins Research Conference, v. 20, p. 16–34, https://doi.org/10.5724/gcs.00.15.00160.5724/gcs.00.15.0016.

Bastianon, E., 2018, Numerical modeling of submarine minibasin flow and morphodynamics [Ph.D. thesis]: Columbia, South Carolina, University of South Carolina, 152 p.

Bastianon, E., Viparelli, E., Cantelli, A., and Imran, J., 2021, 2-D numerical simulation of the filling process of submarine minibasins: Study of deposit architecture: Journal of Sedimentary Research, v. 91, no. 4, p. 399–414, https://doi.org/10.2110/jsr.2020.105.

Beaubouef, R.T., 2004, Deep-water leveed-channel complexes of the Cerro Toro Formation, Upper Cretaceous, southern Chile: AAPG Bulletin, v. 88, no. 11, p. 1471–1500, https://doi.org/10.1306/06210403130.

Beaubouef, R.T., and Abreu, V., 2006, Basin 4 of the Brazos-Trinity slope system: Anatomy of the terminal portion of an intra-slope lowstand systems tract: Gulf Coast Association of Geological Societies Transactions, v. 56, p. 39–49.

Bonnecaze, R.T., Huppert, H.E., and Lister, J.R., 1993, Particle-driven gravity currents: Journal of Fluid Mechanics, v. 250, p. 339–369, https://doi.org/10.1017/S002211209300148X.

De Falco, M., Ottolenghi, L., and Adduce, C., 2020, Dynamics of gravity currents flowing up a slope and implications for entrainment: Journal of Hydraulic Engineering, v. 146, no. 4, https://doi.org/10.1061/(ASCE)HY.1943-7900.0001709.

Dinc, G., Callot, J.-P., and Ringenbach, J.-C., 2023, Shale mobility: From salt-like shale flow to fluid mobilization in gravity-driven deformation, the Late Albian–Turonian White Pointer Delta (Ceduna Subbasin, Great Bight, Australia): Geology, v. 51, p. 174–178, https://doi.org/10.1130/G50611.1.

Dorrell, R.M., Peakall, J., Sumner, E.J., Parsons, D.R., Darby, S.E., Wynn, R.B., Özsoy, E., and Tezcan, D., 2016, Flow dynamics and mixing processes in hydraulic jump arrays: Implications for channel-lobe transition zones: Marine Geology, v. 381, p. 181–193, https://doi.org/10.1016/j.margeo.2016.09.009.

Dorrell, R.M., Patacci, M., and McCaffrey, W.D., 2018, Inflation of ponded, particulate laden density currents: Journal of Sedimentary Research, v. 88, no. 11, p. 1276–1282, https://doi.org/10.2110/jsr.2018.65.

Ellison, T., and Turner, J., 1959, Turbulent entrainment in stratified flows: Journal of Fluid Mechanics, v. 6, no. 3, p. 423–448, https://doi.org/10.1017/S0022112059000738.

Esposito, C.R., Di Leonardo, D., Harlan, M., and Straub, K.M., 2018, Sediment storage partitioning in alluvial stratigraphy: The influence of discharge variability: Journal of Sedimentary Research, v. 88, no. 6, p. 717–726, https://doi.org/10.2110/jsr.2018.36.

Ferguson, R.I., and Church, M., 2004, A simple universal equation for grain settling velocity: Journal of Sedimentary Research, v. 74, no. 6, p. 933–937, https://doi.org/10.1306/051204740933.

Flemings, P.B., Behrmann, J.H., John, C.M., and Expedition Scientists, 2006, Expedition 308 Summary: Integrated Ocean Drilling Program Management International, Inc., for the Integrated Ocean Drilling Program, 362 p.

Fukuda, S., de Vet, M.G., Skevington, E.W., Bastianon, E., Fernández, R., Wu, X., McCaffrey, W.D., Naruse, H., Parsons, D.R., and Dorrell, R.M., 2023, Inadequacy of fluvial energetics for describing gravity current autosuspension: Nature Communications, v. 14, no. 1, 2288, https://doi.org/10.1038/s41467-023-37724-1.

Ge, Z., Gawthorpe, R.L., Rotevatn, A., Zijerveld, L., Jackson, C.A.L., and Oluboyo, A., 2020, Minibasin depocentre migration during diachronous salt welding, offshore Angola: Basin Research, v. 32, no. 5, p. 875–893, https://doi.org/10.1111/bre.12404.

Hamilton, P., Gaillot, G., Strom, K., Fedele, J., and Hoyal, D., 2017, Linking hydraulic properties in supercritical submarine distributary channels to depositional-lobe geometry: Journal of Sedimentary Research, v. 87, no. 9, p. 935–950, https://doi.org/10.2110/jsr.2017.53.

Hudec, M.R., and Jackson, M.P., 2007, Terra infirma: Understanding salt tectonics: Earth-Science Reviews, v. 82, no. 1–2, p. 1–28, https://doi.org/10.1016/j.earscirev.2007.01.001.

Hudec, M.R., Jackson, M.P., and Peel, F.J., 2013, Influence of deep Louann structure on the evolution of the northern Gulf of Mexico: AAPG Bulletin, v. 97, no. 10, p. 1711–1735, https://doi.org/10.1306/04011312074.

Imran, J., Parker, G., and Pirmez, C., 1999, A non-linear model of flow in meandering submarine and subaerial channels: Journal of Fluid Mechanics, v. 400, p. 295–331, https://doi.org/10.1017/S0022112099006515.

Jobe, Z.R., Howes, N., Romans, B.W., and Covault, J.A., 2018, Volume and recurrence of submarine-fan-building turbidity currents: The Depositional Record: The Journal of the International Association of Sedimentologists, v. 4, no. 2, p. 160–176, https://doi.org/10.1002/dep2.42.

Kane, I.A., Clare, M.A., Miramontes, E., Wogelius, R., Rothwell, J.J., Garreau, P., and Pohl, F., 2020, Seafloor microplastic hotspots controlled by deep-sea circulation: Science, v. 368, no. 6495, p. 1140–1145, https://doi.org/10.1126/science.aba5899.

Kramer, K.V., and Shedd, W.W., 2017, A 1.4-billion-pixel map of the Gulf of Mexico seafloor: Eos, v. 98, https://doi.org/10.1029/2017EO073557.

Lamb, M.P., Hickson, T., Marr, J.G., Sheets, B., Paola, C., and Parker, G., 2004, Surging versus continuous turbidity currents: Flow dynamics and deposits in an experimental intraslope minibasin: Journal of Sedimentary Research, v. 74, no. 1, p. 148–155, https://doi.org/10.1306/062103740148.

Lamb, M.P., Toniolo, H., and Parker, G., 2006, Trapping of sustained turbidity currents by intraslope minibasins: Sedimentology, v. 53, p. 147–160, https://doi.org/10.1111/j.1365-3091.2005.00754.x.

Maharaj, V.T., 2012, The effects of confining minibasin topography on turbidity current dynamics and deposit architecture [Ph.D. thesis]: Austin, Texas, University of Texas at Austin, 608 p.

Marini, M., Patacci, M., Felletti, F., and McCaffrey, W., 2016, Fill to spill stratigraphic evolution of a confined turbidite mini-basin succession, and its likely well bore expression: The Castagnola Fm, NW Italy: Marine and Petroleum Geology, v. 69, p. 94–111, https://doi.org/10.1016/j.marpetgeo.2015.10.014.

Mitchell, W.H., Whittaker, A.C., Mayall, M., and Lonergan, L., 2021, New models for submarine channel deposits on structurally complex slopes: Examples from the Niger Delta system: Marine and Petroleum Geology, v. 129, https://doi.org/10.1016/j.marpetgeo.2021.105040.

Mohriak, W.U., Szatmari, P., and Anjos, S., 2012, Salt: Geology and tectonics of selected Brazilian basins in their global context, *in* Alsop, G.I., eds., Salt Tectonics, Sediments and Prospectivity: Geological Society, London, Special Publication 363, p. 131–158, https://doi.org/10.1144/SP363.7.

Mousouliotis, A., Pechlivanidou, S., Albanakis, K., Georgakopoulos, A., and Medvedev, B., 2021, Deciphering salt tectonic deformation patterns in the Eastern Mediterranean: Insights from the Messinian evaporite in the Herodotus Basin: Marine and Petroleum Geology, v. 133, https://doi.org/10.1016/j.marpetgeo.2021.105317.

Parker, G., Garcia, M.H., Fukushima, Y., and Yu, W., 1987, Experiments on turbidity currents over an erodible bed: Journal of Hydraulic Research, v. 25, p. 123–147, https://doi.org/10.1080/00221688709499292.

Patacci, M., Haughton, P.D., and Mccaffrey, W.D., 2015, Flow behavior of ponded turbidity currents: Journal of Sedimentary Research, v. 85, no. 8, p. 885–902, https://doi.org/10.2110/jsr.2015.59.

Pirmez, C., and Imran, J., 2003, Reconstruction of turbidity currents in Amazon Channel: Marine and Petroleum Geology, v. 20, p. 823–849, https://doi.org/10.1016/j.marpetgeo.2003.03.005.

Pirmez, C., Beaubouef, R.T., Friedmann, S.J., and Mohrig, D., 2000, Equilibrium profile and baselevel in submarine channels: Examples from late Pleistocene systems and implications for the architecture of deepwater reservoirs, *in* Weimer, P., ed., Deep-Water Reservoirs of the World: Gulf Coast Section SEPM (Society for Sedimentary Geology) Foundation 20th Annual Bob F. Perkins Research Conference, v. 20, p. 782–805, https://doi.org/10.5724/gcs.00.15.0782.

Pirmez, C., Prather, B.E., Mallarino, G., O'Hayer, W.W., Droxler, A.W., and Winker, C.D., 2012, Chronostratigraphy of the Brazos-Trinity depositional system, western Gulf of Mexico: Implications for deepwater depositional models, *in* Prather, B.E., Deptuck, M.E., Mohrig, D., Van Hoorn, B., and Wynn, R.B., eds., Application of the Principles of Seismic Geomorphology to Continental-Slope and Base-of-Slope Systems: Case Studies from Seafloor and Near-Seafloor Analogues: SEPM (Society for Sedimentary Geology) Special Publication 99, p. 111–143, https://doi.org/10.2110/pec.12.99.0111.

Planchon, O., and Darboux, F., 2002, A fast, simple and versatile algorithm to fill the depressions of digital elevation models: Catena, v. 46, no. 2–3, p. 159–176, https://doi.org/10.1016/S0341-8162(01)00164-3.

Pope, E.L., Cartigny, M.J., Clare, M.A., Talling, P.J., Lintern, D.G., Vellinga, A., Hage, S., Açikalin, S., Bailey, L., and Chapplow, N., 2022a, First source-to-sink monitoring shows dense head controls sediment flux and runout in turbidity currents: Science Advances, v. 8, no. 20, https://doi.org/10.1126/sciadv.abj3220.

Pope, E.L., Heijnen, M.S., Talling, P.J., Jacinto, R.S., Gaillot, A., Baker, M.L., Hage, S., Hasenhündl, M., Heerema, C.J., and McGhee, C., 2022b, Carbon and sediment fluxes inhibited in the submarine Congo Canyon by landslide-damming: Nature Geoscience, v. 15, no. 10, p. 845–853, https://doi.org/10.1038/s41561-022-01017-x.

Prather, B.E., 2003, Controls on reservoir distribution, architecture and stratigraphic trapping in slope settings: Marine and Petroleum Geology, v. 20, no. 6–8, p. 529–545, https://doi.org/10.1016/j.marpetgeo.2003.03.009.

Prather, B.E., Pirmez, C., and Winker, C.D., 2012, Stratigraphy of linked intraslope basins: Brazos–Trinity system western Gulf of Mexico, *in* Prather, B.E., Deptuck, M.E., Mohrig, D., Van Hoorn, B., and Wynn, R.B., eds., Application of the Principles of Seismic Geomorphology to Continental-Slope and Base-of-Slope Sys-

tems: Case Studies from Seafloor and Near-Seafloor Analogues: SEPM (Society for Sedimentary Geology) Special Publication 99, p. 83–109, https://doi.org/10.2110/pec.12.99.0083.

Privat, A.M.L., Peakall, J., Hodgson, D.M., Schwarz, E., Jackson, C.A.L., and Arnol, J.A., 2024, Evolving fill-and-spill patterns across linked early post-rift depocentres control lobe characteristics: Los Molles Formation, Argentina: Sedimentology, v. 71, no. 5, p. 1639–1685.

Reece, J.K., Dorrell, R.M., and Straub, K.M., 2024, Circulation of hydraulically ponded turbidity currents and the filling of continental slope minibasins: Nature Communications, v. 15, no. 1, 2075, https://doi.org/10.1038/s41467-024-46120-2.

Rouse, H., 1939, Experiments on the mechanics of sediment transport, *in* Proceedings of the 5th International Congress for Applied Mechanics: Hoboken, New Jersey, John Wiley, p. 550–554.

Sequeiros, O.E., Spinewine, B., Garcia, M.H., Beaubouef, R.T., Sun, T., and Parker, G., 2009, Experiments on wedge-shaped deep sea sedimentary deposits in minibasins and/or on channel levees emplaced by turbidity currents. Part I. Documentation of the flow: Journal of Sedimentary Research, v. 79, no. 8, p. 593–607, https://doi.org/10.2110/jsr.2009.064.

Sequeiros, O.E., Spinewine, B., Beaubouef, R.T., Sun, T., García, M.H., and Parker, G., 2010, Characteristics of velocity and excess density profiles of saline underflows and turbidity currents flowing over a mobile bed: Journal of Hydraulic Engineering, v. 136, no. 7, p. 412–433, https://doi.org/10.1061/(ASCE)HY.1943-7900.0000200.

Shcherbina, A.Y., D'Asaro, E.A., and Nylund, S., 2018, Observing finescale oceanic velocity structure with an autonomous Nortek acoustic Doppler current profiler: Journal of Atmospheric and Oceanic Technology, v. 35, no. 2, p. 411–427, https://doi.org/10.1175/JTECH-D-17-0108.1.

Shields, M.R., Bianchi, T.S., Mohrig, D., Hutchings, J.A., Kenney, W.F., Kolker, A.S., and Curtis, J.H., 2017, Carbon storage in the Mississippi River delta enhanced by environmental engineering: Nature Geoscience, v. 10, no. 11, p. 846–851, https://doi.org/10.1038/ngeo3044.

Simmons, S., Azpiroz-Zabala, M., Cartigny, M., Clare, M., Cooper, C., Parsons, D., Pope, E., Sumner, E., and Talling, P., 2020, Novel acoustic method provides first detailed measurements of sediment concentration structure within submarine turbidity currents: Journal of Geophysical Research: Oceans, v. 125, no. 5, https://doi.org/10.1029/2019JC015904.

Smith, R., 2004, Turbidite systems influenced by structurally induced topography in the multi-sourced Welsh Basin, *in* Lomas, S.A., and Joseph, P., eds., Confined Turbidite Systems: Geological Society, London, Special Publication 222, p. 209–228, https://doi.org/10.1144/GSL.SP.2004.222.01.11.

Soto, J.I., Heidari, M., and Hudec, M.R., 2021, Proposal for a mechanical model of mobile shales: Scientific Reports, v. 11, 23785, https://doi.org/10.1038/s41598-021-02868-x.

Steffens, G.S., Biegert, E.K., Sumner, H.S., and Bird, D., 2003, Quantitative bathymetric analyses of selected deepwater siliciclastic margins: Receiving basin configurations for deepwater fan systems: Marine and Petroleum Geology, v. 20, no. 6–8, p. 547–561, https://doi.org/10.1016/j.marpetgeo.2003.03.007.

Straub, K.M., and Mohrig, D., 2009, Constructional canyons built by sheet-like turbidity currents: Observations from offshore Brunei Darussalam: Journal of Sedimentary Research, v. 79, no. 1, p. 24–39, https://doi.org/10.2110/jsr.2009.006.

Stricker, S., Jones, S.J., Meadows, N., and Bowen, L., 2018, Reservoir quality of fluvial sandstone reservoirs in salt-walled mini-basins: An example from the Seagull field, Central Graben, North Sea, UK: Petroleum Science, v. 15, no. 1, p. 1–27, https://doi.org/10.1007/s12182-017-0206-x.

Talling, P.J., Allin, J., Armitage, D.A., Arnott, R.W., Cartigny, M.J., Clare, M.A., Felletti, F., Covault, J.A., Girardclos, S., and Hansen, E., 2015, Key future directions for research on turbidity currents and their deposits: Journal of Sedimentary Research, v. 85, no. 2, p. 153–169, https://doi.org/10.2110/jsr.2015.03.

Talling, P.J., Baker, M.L., Pope, E.L., Ruffell, S.C., Jacinto, R.S., Heijnen, M.S., Hage, S., Simmons, S.M., Hasenhündl, M., and Heerema, C.J., 2022, Longest sediment flows yet measured show how major rivers connect efficiently to deep sea: Nature Communications, v. 13, 4193, https://doi.org/10.1038/s41467-022-31689-3.

Talling, P.J., Hage, S., Baker, M.L., Bianchi, T.S., Hilton, R.G., and Maier, K.L., 2024, The global turbidity current pump and its implications for organic carbon cycling: Annual Review of Marine Science, v. 16, p. 105–133, https://doi.org/10.1146/annurev-marine-032223-103626.

Toniolo, H., Lamb, M., and Parker, G., 2006a, Depositional turbidity currents in diapiric minibasins on the continental slope: Formulation and theory: Journal of Sedimentary Research, v. 76, no. 5, p. 783–797, https://doi.org/10.2110/jsr.2006.071.

Toniolo, H., Parker, G., Voller, V., and Beaubouef, R., 2006b, Depositional turbidity currents in diapiric minibasins on the continental slope: Experiments—Numerical simulation and upscaling: Journal of Sedimentary Research, v. 76, no. 5, p. 798–818, https://doi.org/10.2110/jsr.2006.072.

Tucker, C.J., 1979, Red and photographic infrared linear combinations for monitoring vegetation: Remote Sensing of Environment, v. 8, no. 2, p. 127–150, https://doi.org/10.1016/0034-4257(79)90013-0.

van Rensbergen, P., Morley, C.K., Ang, D.W., Hoan, T.Q., and Lam, N.T., 1999, Structural evolution of shale diapers from reactive rise to mud volcanism: 3-D seismic data from the Baram delta, offshore Brunei Darussalam: Journal of the Geological Society, v. 156, p. 633–650, https://doi.org/10.1144/gsjgs.156.3.0633.

Vendettuoli, D., Clare, M., Clarke, J.H., Vellinga, A., Hizzet, J., Hage, S., Cartigny, M., Talling, P., Waltham, D., and Hubbard, S., 2019, Daily bathymetric surveys document how stratigraphy is built and its extreme incompleteness in submarine channels: Earth and Planetary Science Letters, v. 515, p. 231–247, https://doi.org/10.1016/j.epsl.2019.03.033.

Violet, J., Sheets, B., Pratson, L., Paola, C., Beaubouef, R.T., and Parker, G., 2005, Experiment on turbidity currents and their deposits in a model 3-D subsiding minibasin: Journal of Sedimentary Research, v. 75, no. 5, p. 820–843, https://doi.org/10.2110/jsr.2005.065.

Wahab, A., Hoyal, D.C., Shringarpure, M., and Straub, K.M., 2022, A dimensionless framework for predicting submarine fan morphology: Nature Communications, v. 13, 7563, https://doi.org/10.1038/s41467-022-34455-7.

Wang, L., and Liu, H., 2006, An efficient method for identifying and filling surface depressions in digital elevation models for hydrologic analysis and modelling: International Journal of Geographical Information Science, v. 20, no. 2, p. 193–213, https://doi.org/10.1080/13658810500433453.

Winker, C.D., 1996, High-resolution seismic stratigraphy of a late Pleistocene submarine fan ponded by salt-withdrawal mini-basins on the Gulf of Mexico continental slope, *in* Proceedings, Offshore Technology Conference, Houston, Texas, 6–9 May: OnePetro, OTC-8024-MS, p. 619–628, https://doi.org/10.4043/8024-MS.

Winker, C.D., and Booth, J.R., 2000, Sedimentary dynamics of the salt-dominated continental slope, Gulf of Mexico: Integration of observations from the seafloor, near-surface, and deep subsurface, *in* Weimer, P., ed., Deep-Water Reservoirs of the World: Gulf Coast Section SEPM (Society for Sedimentary Geology) Foundation 20th Annual Bob F. Perkins Research Conference, v. 20, p. 1059–1086, https://doi.org/10.5724/gcs.00.15.1059.

Xu, J.P., Nobel, M.A., and Rosenfeld, L.K., 2004, In-situ measurements of velocity structure within turbidity currents: Geophysical Research Letters, v. 31, no. 9, https://doi.org/10.1029/2004GL019718.

Zucker, E., Gvirtzman, Z., Steinberg, J., and Enzel, Y., 2020, Salt tectonics in the Eastern Mediterranean Sea: Where a giant delta meets a salt giant: Geology, v. 48, p. 134–138, https://doi.org/10.1130/G47031.1.

Science Editor: Troy Rasbury
Associate Editor: Alexander Whittaker

Manuscript Received 19 December 2023
Revised Manuscript Received 30 September 2024
Manuscript Accepted 24 October 2024